1   An Emerging Aerosol Climatology via Remote Sensing over Metro Manila, Philippines
2
3   Genevieve Rose Lorenzo[1,2], Avelino F. Arellano[1], Maria Obiminda Cambaliza[2,3], Christopher
4   Castro[1], Melliza Templonuevo Cruz[2,4], Larry Di Girolamo[5], Glenn Franco Gacal[2], Miguel
5   Ricardo A. Hilario[1], Nofel Lagrosas[6], Hans Jarett Ong[2], James Bernard Simpas[2,3], Sherdon Niño
6   Uy[2], and Armin Sorooshian[1,7]
7
8   [1]Department of Hydrology and Atmospheric Sciences, University of Arizona, Tucson, Arizona,
9   85721, USA
10   [2]Air Quality Dynamics-Instrumentation & Technology Development Laboratory, Manila
11   Observatory, Quezon City, 1108, Philippines
12   [3]Department of Physics, School of Science and Engineering, Ateneo de Manila University,
13   Quezon City, 1108, Philippines
14   [4]Institute of Environmental Science and Meteorology, University of the Philippines, Diliman,
15   Quezon City, 1101, Philippines
16   [5]Department of Atmospheric Science, University of Illinois, Urbana-Champlain, Illinois, 61801,
17   USA
18   [6]Center for Environmental Remote Sensing, Chiba University, Chiba, 263-8522, Japan
19   [7]Department of Chemical and Environmental Engineering, University of Arizona, Tucson,
20   Arizona, 85721, USA
21
22   *Correspondence to:* armin@arizona.edu

23 **Abstract**

24 Aerosol particles in Southeast Asia are challenging to characterize due to their complex life cycle
25 within the diverse topography and weather in the region. An emerging aerosol climatology was
26 established based on AERONET data (December 2009 to October 2018) for clear sky days in
27 Metro Manila, Philippines. Aerosol optical depth (AOD) values were highest from August to
28 October, partly from fine urban aerosol particles, including soot, coinciding with the burning
29 season in Insular Southeast Asia when smoke is often transported to Metro Manila during the
30 southwest monsoon. Clustering of AERONET volume size distributions (VSD) resulted in five
31 aerosol particle sources based on the position and magnitude of their peaks in the VSD and the
32 contributions of specific particle species to AOD per cluster based on MERRA-2. The clustering
33 showed that the majority of aerosol particles above Metro Manila were from a clean marine
34 source (58%), which could be related to AOD values there being relatively smaller than in other
35 cities in the region. The following are the other particle sources over Metro Manila: fine polluted
36 (20%), mixed dust (12%), urban/industrial (5%), and cloud processing (5%). Furthermore,
37 MERRA-2 AOD data over Southeast Asia were analyzed using empirical orthogonal functions.
38 Along with AOD fractional compositional contributions and wind regimes, four dominant
39 aerosol particle air masses emerged: two sulfate air masses from East Asia, an organic carbon
40 source from Indonesia, and a sulfate source from the Philippines. Knowing the local and regional
41 aerosol particle air masses that impact Metro Manila is useful in identifying the sources while
42 gaining insight on how aerosol particles are affected by long-range transport and their impact on
43 regional weather.

1. Introduction

Although Southeast Asia is one of the most rapidly developing regions in the world with a growing number of extensive research conducted (Reid et al., 2023), there remain knowledge gaps related to aerosol particles in the area (Tsay et al., 2013; Lee et al., 2018; Chen et al., 2020; Amnuaylojaroen, 2023). The region represents a complex geographic, meteorological, and hydrological environment making it challenging to understand aerosol particle characteristics, especially interactions between aerosol particles with their environment (Reid et al., 2013). The island of Luzon in the Philippines in particular is very populated and is characterized by high levels of anthropogenic emissions superimposed on natural emissions from the surrounding waters (AzadiAghdam et al., 2019) and long-range transport of emissions from areas such as Indonesia and East Asia (Braun et al., 2020; Hilario et al., 2020a; Hilario et al., 2020b; Hilario et al., 2021a). Aerosol particle lifecycle in the region is impacted by Philippine weather that is marked by two distinct monsoons, typhoons, the intertropical convergent zone, and impacts from El Niño-Southern Oscillation and Madden-Julian Oscillation (Cruz et al., 2013; Xian et al., 2013; Reid et al., 2012; Reid et al., 2015; Hilario et al., 2021b). Studying this area is informative owing to the wide dynamic range of aerosol particle and weather conditions, which are interconnected. The overlapping of large fraction of cirrus clouds with lower clouds in the area (Hong and Di Girolamo, 2020) makes space-borne remote sensing of aerosol particles very challenging (Reid et al., 2013; Lin et al., 2014). These reasons motivated the NASA Cloud, Aerosol, and Monsoon Processes Philippines Experiment (CAMP^{2}Ex) airborne measurement campaign in 2019 to understand the interaction between tropical meteorology and aerosol particles (Di Girolamo et al., 2015; Reid et al., 2023). However, those short terms measurements cannot provide an adequate assessment of aerosol behavior across all seasons and over many years.

The NASA AErosol RObotic NETwork (AERONET) (Holben et al., 1998) is pivotal in providing broad temporal coverage of aerosol characteristics in specific locations with a column-based perspective from the ground up. Aerosol climatology studies in different regions have proved beneficial to understand temporal characteristics of aerosol particle concentrations and properties, in addition to identifying potential source regions along with interactions with clouds and rainfall (Stevens and Feingold, 2009; Li et al., 2011; Tao et al., 2012; Crosbie et al., 2014; Kumar et al., 2015; Alizadeh-Choobari and Gharaylou, 2017; Mora et al., 2017; Aldhaif et al., 2021). To our knowledge, there has not been a remote sensing-based aerosol climatology study for the Metro Manila region of Luzon, which has approximately 16 cities, a population of 12.88 million, and a high population density of 20,800 km^{-2} (PSA, 2016; Alas et al., 2018).

Most of the past studies involving long-term remotely sensed aerosol particle data in Southeast Asia (Cohen, 2014; Nakata et al., 2018; Nguyen et al., 2019b) had no specific focus on the Philippines. The Philippines is considered as part of the Maritime Continent (MC), the island nations sub-region of Southeast Asia. The other Southeast Asia sub-region, Peninsular Southeast Asia (PSEA), comprises those nations within the continental Asia land mass. These two regions have separate aerosol sources and climate, where MC is dependent on the intertropical convergent zone (ITCZ) and PSEA is dependent on both the ITCZ and monsoon systems (Dong and Fu, 2015). Only the southern part of the Philippines is climatologically part of MC (Ramage, 1971), however, and northwest Philippines, where Metro Manila is located, is affected by the monsoons and tropical cyclones aside from the ITCZ (Chang et al., 2005; Yumul Jr et al., 2010; Bagtasa, 2017). These unique meteorological influences and extensive local aerosol particle

3

88 sources warrant a unique aerosol climatology over Metro Manila, one of a polluted source in a
89 tropical marine environment, and its effects on cloud formation in the area. Aerosol effects on
90 clouds in the marine environment are associated with the largest uncertainties in climate change
91 research (Hendrickson et al., 2021; Wall et al., 2022) and the Philippines was ranked as the 5th
92 country globally as most at risk to climate change and extreme weather from 1997 to 2018
93 (Eckstein et al., 2018). There have been several surface measurements of aerosol particles made
94 in Metro Manila for the past 20 years (Oanh et al., 2006; Bautista VII et al., 2014; Cruz et al.,
95 2019) but columnar ground-based measurements there are just beginning to be established
96 (Dorado et al., 2001; Ong et al., 2016; Cruz et al., 2023). The AERONET sun photometer is one
97 of the first long-term column-based aerosol instruments in Metro Manila and the Philippines
98 (Ong et al., 2016).

99 The goal of this study is to use multi-year AERONET data in Manila Observatory along with
100 other complementary datasets (MERRA-2, PERSIANN, MISR, HYSPLIT, and NAAPS) to
101 address the following questions: (1) what are the monthly characteristics of aerosol particles over
102 Metro Manila, Philippines?; (2) what are the possible sources and factors influencing the
103 observed characteristics?; (3) what relationships are evident between aerosol particles and cloud
104 characteristics?; and (4) what are the regional and local aerosol particle air masses that influence
105 Metro Manila?
106
107 **2. Methods**

108 This work relies on analysis of several datasets summarized in Table 1 and the following
109 subsections. The common time range used for all datasets is between January 2009 and October
110 2018.

111 **Table 1:** Summary of datasets over Metro Manila used in this work covering the period from
112 January 2009 to October 2018.

Parameter	Data Source	Spatial Coverage	Time Coverage
Aerosol Optical Depth (500 nm)	AERONET	14.635° N, 121.078° E	Jan 2009 - Oct 2018
Asymmetry Factor (440 nm - 1020 nm)	AERONET	14.635° N, 121.078° E	Jan 2009 - Oct 2018
Extinction Angstrom Exponent (440 nm -870 nm)	AERONET	14.635° N, 121.078° E	Jan 2009 - Oct 2018
Fine Mode Fraction	AERONET	14.635° N, 121.078° E	Jan 2009 - Oct 2018
Precipitable Water	AERONET	14.635° N, 121.078° E	Jan 2009 - Oct 2018
Single Scattering Albedo (440 nm - 1020 nm)	AERONET	14.635° N, 121.078° E	Jan 2009 - Oct 2018
Refractive Index (Real and Imaginary; 440 nm - 1020 nm)	AERONET	14.635° N, 121.078° E	Jan 2009 - Oct 2018
Volume Size Distribution	AERONET	14.635° N, 121.078° E	Jan 2009 - Oct 2018
Low Cloud Fraction (MODIS)	MERRA-2	14.3° N - 14.8° N, 120.75° E - 121.25° E	Jan 2009 - Oct 2018
Planetary Boundary Layer Height	MERRA-2	14.3° N - 14.8° N, 120.75° E - 121.25° E	Jan 2009 - Oct 2018

Relative Humidity (975 mb)	MERRA-2	14.3° N - 14.8° N, 120.75° E - 121.25° E	Jan 2009 - Oct 2018
Sea Level Pressure	MERRA-2	14.3° N - 14.8° N, 120.75° E - 121.25° E	Jan 2009 - Oct 2018
Temperature (975 mb)	MERRA-2	14.3° N - 14.8° N, 120.75° E - 121.25° E	Jan 2009 - Oct 2018
Wind (975 mb)	MERRA-2	14.3° N - 14.8° N, 120.75° E - 121.25° E	Jan 2009 - Oct 2018
Total Extinction Aerosol Optical Depth (550 nm)	MERRA-2	14.3° N - 14.8° N, 120.75° E - 121.25° E	Jan 2009 - Oct 2018
Sulfate, Black Carbon, Organic Carbon, Dust, and Sea Salt Extinction Aerosol Optical Depth (550 nm)	MERRA-2	14.3° N - 14.8° N, 120.75° E - 121.25° E	Jan 2009 - Oct 2018
Precipitation	PERSIANN	14.3° N - 14.8° N, 120.75° E - 121.25° E	Jan 2009 - Oct 2018

2.1 Datasets

2.1.1 AERONET

The central dataset used is that of sun photometer measurements and derived (inversion) parameters from the AERONET (Holben et al., 1998) site at the Manila Observatory in Quezon City, Philippines (14.64° N, 121.08° E, ~70 m. a. s. l.). Direct sunlight extinction measurements were made at nominal wavelengths of 340, 380, 440, 500, 675, 870, 940, and 1020 nm, from which aerosol optical depth (AOD) was calculated (except for 940 nm, which is for water vapor) (Eck et al., 2013). AOD is a commonly used proxy for aerosol particle loading in the air column from the ground up (Holben et al., 2001); higher AOD translates to more aerosol particle extinction in the column above a location. The extinction angstrom exponent (EAE) and the fine mode fraction (FMF) are also AERONET direct sun products that are retrieved after the application of a spectral de-convolution algorithm (O'Neill et al., 2003). For the inversion products, it is through radiative retrievals that the volume size distribution (VSD) and complex refractive index (RI) are gathered and from which single scattering albedo (SSA) and asymmetry factor (AF) are calculated. The AERONET observations were made during clear sky conditions, which has been shown (Hong and Di Girolamo, 2022) to be able to represent all sky conditions.

For the inversions, four wavelengths (440, 670, 870, and 1020 nm) of the radiometer spectral channels were chosen for diffuse radiance measurements and to avoid gas absorption (Dubovik et al., 1998). Version 3 Direct Sun and Inversion algorithms (AERONET, 2019; Giles et al., 2019) were used with the Almucantar Sky Scan Scenario to derive the following parameters with level 2.0 (automatically cloud-cleared and quality controlled datasets with pre- and post-field calibrations) data quality: column AOD (500 nm), fine mode fraction (500 nm), extinction angstrom exponent (440 – 870 nm), precipitable water (940 nm), single scattering albedo (440, 670, 870, and 1020 nm), asymmetry factor (440, 670, 870, and 1020 nm), refractive index (440, 670, 870, and 1020 nm), and VSD. The version 3 products are able to keep fine mode aerosol particle data (haze and smoke) as well as remove optically thin cirrus clouds in order to retain more aerosol particle measurements in the database (Giles et al., 2019). Cloud screening in the version 3 product improves remote sensing measurements in Southeast Asia in general, where cirrus clouds are pervasive (Reid et al., 2013). At most, a total of 29,037 direct sun and 1419 inversion AERONET daytime data points were available between January 2009 and October 2018.

2.1.2 MERRA-2

145   Modern Era-Retrospective Analysis for Research and Applications, Version 2 (MERRA-2: 0.5°
146   × 0.625° approximate resolution) meteorological and aerosol particle composition reanalysis data
147   (Bosilovich, 2016; Gelaro et al., 2017; Randles et al., 2017) were acquired for the area around
148   Manila Observatory (14.25° N – 14.75° N, 120.9375° E – 121.5625° E). The aerosol reanalysis
149   data includes data assimilation of AOD from the Moderate Resolution Imaging
150   Spectroradiometer (MODIS: Terra, 2000 to present and Aqua, 2002 to present), Advanced Very
151   High Resolution Radiometer (AVHRR, 1979-2002), and Multiangle Imaging SpectroRadiometer
152   (MISR, 2000-2014) (Buchard et al., 2017; Rizza et al., 2019). The following products were used:
153   M2I3NPASM Assimilated Meteorological Fields (3-hourly) for 975 mb level winds,
154   temperature, relative humidity, and sea level pressure; M2T1NXFLX Surface Flux Diagnostics
155   (1-hourly from 00:30 UTC time-averaged) 2D for planetary boundary layer height;
156   M2T1NXCSP COSP Satellite Simulator (1-hourly from 00:30 UTC time-averaged) for MODIS
157   mean low cloud fraction (cloud top pressure > 680 hPa); and M2T1NXAER Aerosol Diagnostics
158   (1-hourly from 00:30 UTC time-averaged) for Total AOD and speciated AOD (Sulfate, Black
159   Carbon (BC), Organic Carbon (OC), Dust, and Sea Salt).

160   MERRA-2 meteorological and aerosol particle composition monthly mean reanalysis data
161   (Bosilovich, 2016; Gelaro et al., 2017; Randles et al., 2017) were also acquired for a larger
162   region (30° × 30°), the Southeast Asia region (0° N – 30° N, 105° E – 135° E) for the period
163   from January 2009 to December 2018. This is within the spatial domain of the CAMP^{2}Ex
164   airborne measurement campaign which, as mentioned earlier, targets the interaction between
165   tropical meteorology and aerosol particles. The following datasets (0.5° latitude and 0.625°
166   longitude resolution) were used: MERRA-2 tavgM_2d_aer_Nx: Aerosol Assimilation
167   (M2TMNXAER) for Total 500 nm AOD and speciated 500 nm AOD (Sulfate, BC, OC, Dust,
168   and Sea Salt) and MERRA-2 instM_3d_ana_Np: Analyzed Meteorological Fields
169   (M2IMNPANA) for 1000 hPa and 725 hPa level U and V winds. The total MERRA-2 AOD
170   (reanalysis) for the region (mean over 30° x 30° region) was used along with MISR AOD
171   (remote sensing) data (mean over 30° x 30° region) to assess the influence of long-range sources
172   to the aerosol column over Manila Observatory. The monthly meteorological and aerosol particle
173   composition data for the region will be used for empirical orthogonal functions, which will be
174   described later.

175   2.1.3 PERSIANN
176   Hourly precipitation data were obtained from the Precipitation Estimation from the Remotely
177   Sensed Information using Artificial Neural Networks (PERSIANN) database of the Center for
178   Hydrometeorology and Remote Sensing (CHRS) at the University of California, Irvine (UCI).
179   Hourly data were accumulated for running three-day totals, which were compared to AERONET
180   data. The data were averaged between the four grids that included the area of interest as well as
181   ensuring a similar spatial domain (14.5° N – 15.0° N, 120.75° E – 121.25° E) to the MERRA-2
182   dataset.

183   2.1.4 MISR
184   Monthly 500 nm AOD data (Level 3 Global Aerosol: 0.5° × 0.5° spatial resolution in the region
185   0.25° N – 30.25° N and 104.75° E – 134.75° E) from January 2009 to December 2018 are used
186   from the Multi-angle Imaging SpectroRadiometer (MISR), (Diner et al., 2007; Garay et al.,
187   2018) as regional (Southeast Asia) baseline remote sensing data to support the Manila
188   Observatory AERONET data. The regional (30° × 30°) MISR data was used to confirm regional

189 sources of aerosols that may be influencing the AOD over Metro Manila. Level 3 MISR products
190 are global maps of parameters available in Level 2 (measurements derived from the instrument
191 data) products. MISR is ideal for remote sensing in the CAMP^{2}Ex region because it has an
192 overpass at 10:30 AM ECT (descending mode) (when cirrus is minimal) and its retrievals have
193 been shown to be unimpacted by small cumulus (Zhao et al., 2009), which are typical in the
194 region. MISR has relatively more accurate AOD and agrees better with AERONET data
195 compared to other satellite products due to its multi-angle measurements (Choi et al., 2019;
196 Kuttippurath and Raj, 2021). The MISR sampling noise is relatively small due to the large
197 domain and seasonal averages that are considered in this study. MISR is also the only passive
198 sensor that speciates aerosol particle size and shape. All these factors led to the choice of using
199 regional MISR data to associate long-range sources influencing AERONET data in Manila
200 Observatory. Monthly mean AOD (bin 0) were extracted for Southeast Asia (0.25° N – 30.25°
201 N, 104.75° E – 134.75° E) within the CAMP^{2}Ex region. Monthly mean AOD values were then
202 calculated for each 0.5° grid point and then for the $30° \times 30°$ region, where the standard error in
203 the monthly mean for the region is less than 0.002. MISR monthly mean time series of size,
204 shape, and absorption speciated 550 nm AOD and angstrom exponent in the CAMP^{2}Ex domain
205 (6.5° N – 22.5° N, 116.5° E – 128.5° E; March 2000 to December 2020) are also used to support
206 the findings from the AERONET data.

207 2.1.5 NAAPS
208 Archived maps of total and speciated optical depths and surface concentrations of sulfate, dust,
209 and smoke for Southeast Asia are used from the Navy Aerosol Analysis and Prediction System
210 (NAAPS: $1° \times 1°$ spatial resolution) (Lynch et al., 2016), and which are publicly available at
211 https://www.nrlmry.navy.mil/aerosol/. This reanalysis product relies on the Navy Global
212 Environmental Model (NAVGEM) for meteorological fields (Hogan et al., 2014). Hourly maps
213 were downloaded for aerosol particle events of interest based on AERONET data. These maps
214 help associate possible regional emission sources to extreme aerosol loading events in Manila
215 Observatory. Previous studies have used NAAPS data for an overview of aerosol sources in
216 specific regions of interest (Ross et al., 2018; Foth et al., 2019; Markowicz et al., 2021; Harenda
217 et al., 2022; Mims III, 2022). More recent studies show the need to improve aerosol
218 representation in NAAPS (Edwards et al., 2022), so we will use NAAPS qualitatively, together
219 with MERRA-2 compositional AOD data and back-trajectories, for an overview of aerosol
220 sources that may contribute to extreme events with high AOD from AERONET.

221 2.1.6 HYSPLIT
222 Back-trajectories from the National Oceanic and Atmospheric Administration's (NOAA) Hybrid
223 Single-Particle Lagrangian Integrated Trajectory (HYSPLIT) model (Stein et al., 2015; Rolph et
224 al., 2017) were used to provide support for the AERONET monthly aerosol characteristics and
225 the chosen case studies. Three and seven-day back-trajectories with six-hour resolution were
226 generated based on the NCEP/NCAR reanalysis meteorological dataset and with a resolution of
227 1° and a vertical wind setting of "model vertical velocity". The three-day data were used to map
228 the density of trajectories reaching Manila Observatory in each month from 2008 to 2019. The
229 seven-day data were used in the analysis of the case studies. Trajectories were computed for an
230 end point with an altitude of 500 m above ground level at the Manila Observatory. This altitude
231 represents the mixed layer based on related surface air quality studies (Crosbie et al., 2014; Mora
232 et al., 2017; Schlosser et al., 2017; Aldhaif et al., 2020), including a previous study for the same
233 area (Stahl et al., 2020).

234 2.1.7 NASA Worldview
235 Archived maps of cloud fraction (Aqua MODIS and Terra MODIS) over Metro Manila and
236 Southeast Asia were downloaded from NASA Worldview (https://worldview.earthdata.nasa.gov)
237 for events of interest based on AERONET data.
238
239 **2.2 Clustering**
240 Available AERONET VSD data (0.050 µm to 15.000 µm particle radius in 22 logarithmically
241 equidistant discrete points, 1419 data points) were clustered via k-means clustering (Lloyd,
242 1982). The algorithm used was k-means++ (Arthur and Vassilvitskii, 2006). The ideal number
243 of clusters was chosen based on relatively highest (>0.5) average silhouette value and the
244 presence of a cluster with a second peak in the larger accumulation mode of the VSD. The
245 clusters were analyzed based on their associated meteorological conditions and aerosol particle
246 characteristics and were classified into air mass types (Table 2) based on estimates from previous
247 studies (Dubovik et al., 2002; Pace et al., 2006; Kaskaoutis et al., 2007; Kaskaoutis et al., 2009;
248 Sorooshian et al., 2013; Kumar et al., 2014; Sharma et al., 2014; Che et al., 2015; Kumar et al.,
249 2015; Deep et al., 2021). The first four mentioned air mass types in Table 2 are the most general,
250 and four more classifications based on aerosol particle sources are included. The urban/industrial
251 air mass type here refers to local combustion along with long-range transported biomass burning
252 (Kaskaoutis et al., 2009). While these classifications are not rigid definitions of air masses, they
253 help in understanding the sources that contribute to aerosols in Metro Manila and in identifying
254 cases where certain sources are more influential than others.

255 **Table 2:** Summary of threshold values of aerosol optical depth (AOD), angstrom exponent (AE),
256 fine mode fraction (FMF), and single scattering albedo (SSA) used to identify air mass types.

Air Mass Type	AOD	AE	FMF	SSA	Source
Clean Fine	< 0.1[a]	> 1[a]	> 0.7[a]	-	Sorooshian et al., 2013
Polluted Fine	> 0.1[a]	> 1[a]	> 0.7[a]	-	Sorooshian et al., 2013
Clean Coarse	< 0.1[a]	< 1[a]	< 0.3[a]	-	Sorooshian et al., 2013
Polluted Coarse	> 0.1[a]	< 1[a]	< 0.3[a]	-	Sorooshian et al., 2013
Clean Marine	< 0.2[b]	< 0.9[d]	-	0.98[e]	Kaskaoutis et al., 2009 Dubovik et al., 2002
Urban/Industrial	> 0.2[b]	> 1[d]	-	0.9-0.98[e]	Kaskaoutis et al., 2009 Dubovik et al., 2002
Biomass Burning	-	> 1.4[a]	-	0.89-0.95[e]	Deep et al., 2021 Dubovik et al., 2002
Desert Dust	> 0.3[c]	< 1[d]	-	0.92-0.93[e]	Kaskaoutis et al., 2009 Deep et al., 2021 Dubovik et al., 2002

[a] from MODIS   [c] AOD at 400 nm   [e] SSA at 440 nm

[b] AOD at 500 nm   [d] AE at 380 nm to 870 nm

257

2.3 Extreme Event Analysis

Aerosol particle events based on the three clusters with the highest VSD concentrations were identified to characterize different types of sources and processes impacting aerosol particle columnar properties above Metro Manila. The three events are described below.

2.3.1   Smoke Long Range Transport

Events related to transported biomass burning/smoke were chosen from the AERONET VSD data that were clustered as urban/industrial (with a dominant submicrometer peak) (Eck et al., 1999) over Metro Manila. Cases with the highest black carbon contribution to total AOD from the MERRA-2 dataset were considered. Maps from NAAPS of high smoke contributions to AOD and surface smoke contributions in the direction of back-trajectories HYSPLIT were used to provide support for the likely source and transport pathway for the smoke cases.

2.3.2   Dust Long Range Transport

A dust transport case over Metro Manila was identified from the AERONET VSD dust cluster (with an enhanced coarse peak in the AERONET VSD compared to the submicrometer fraction) (Eck et al., 1999), the highest dust contribution to AOD from the MERRA-2 dataset, and high dust contributions to AOD from NAAPS. Surface dust concentrations from NAAPS along the HYSPLIT back-trajectories improved the plausibility of dust for this case.

2.3.3   Cloud Processing

Cloud processing events were identified based on bimodal submicrometer VSDs (Eck et al., 2012) and a relatively large sulfate contribution to AOD over Metro Manila from the MERRA-2 dataset, since this species is predominantly produced via cloud processing (Barth et al., 2000; Faloona, 2009). The presence of clouds was verified qualitatively with MODIS (Aqua and Terra) imagery from NASA Worldview in the path of air parcels reaching Metro Manila based on HYSPLIT back-trajectories.

2.4 Empirical Orthogonal Functions

Regional analysis of aerosol particles in Southeast Asia and Asia in general show the prevalence of biomass burning in the region, as well as the larger influence of anthropogenic emissions in East Asia (Nakata et al., 2018). These large prevalent sources may overshadow other relevant but weaker sources in the region, such as local sources. Due to the complex nature of aerosol particles, analysis techniques such as principal component analysis and clustering along with recent improvements in gridded datasets help detect spatial and temporal patterns that would otherwise be difficult to make with noise interference and even weak signals (Li et al., 2013; Sullivan et al., 2017; Plymale et al., 2021). Understanding the dominant air masses around Southeast Asia will help in distinguishing local and transported particles that influence the aerosol climatology in Metro Manila.

To contextualize the analysis of aerosol particle masses in Metro Manila, major regional sources of aerosol particles in Southeast Asia were identified based on the dominant principal components from empirical orthogonal (EOF) analysis of AOD. EOF analysis was done on the monthly AOD data (January 2009 to December 2018) from MERRA-2 for the Southeast Asia region for the months similar in scope to the AERONET data. EOF analysis needs a complete

299   dataset with no data gaps, which is not available with pure satellite retrievals like MISR; the
300   MERRA-2 reanalysis dataset alleviates this issue.

301   The monthly MERRA-2 AOD maps (0° - 30° N, 105° E – 135° E with 0.5° latitude and 0.625°
302   longitude resolution) (Lat: 61 rows x Lon: 49 columns) for the Southeast Asia region (presented
303   subsequently) were first deseasonalized. Then, the AOD anomaly per grid per year (of the 120
304   months) was calculated by subtracting the monthly mean AOD from each value of a given month
305   (Li et al., 2013). The anomalies per grid were weighted depending on their latitude by
306   multiplying the anomalies by the square root of the cosine of their latitudes.

307   EOF, specifically singular value decomposition (SVD), analysis (Björnsson and Venegas, 1997)
308   was then performed. To prepare the data for the analysis, they were transformed such that the
309   final matrix was a 2D matrix (120 x 2989) with each row representing a year, and each column
310   representing a grid in the map. The matrix was analyzed for eigenvalues using SVD in Matlab,
311   which outputs the eigenvalue (S) and eigenvector (U: principal components and V: empirical
312   orthogonal functions) matrices. The eigenvalues were, by default, arranged in descending order.
313   Each principal component (PC) time series was standardized by dividing each PC value by the
314   standard deviation per PC time series (120 months).

315   An eigenvalue spectrum was also plotted based on the variance explained by each eigenvalue
316   and error bars that were calculated using the North test (North et al., 1982). Then, the
317   unweighted AOD anomalies were regressed onto the first three standardized PCs. Each grid
318   therefore had a regression between 120 pairs (unweighted AOD anomalies vs standardized PCs).
319   From the linear regression equation, the regression coefficient per grid was calculated. Each grid
320   on the Southeast Asia map was colored based on the calculated regression coefficient value.
321
322   **2.5 Correlations**
323   The first three standardized PCs of AOD anomalies were correlated to deseasonalized
324   compositional AOD fractions (Sulfate, BC, OC, Dust, and Sea Salt) from MERRA-2. For each
325   correlation, the t-test value was calculated, and the resulting t-score was compared to a t-critical
326   value for ~n= 100 pairs (n is the number of pairs of data, in this case 120 months) for 0.90
327   confidence level, which is 1.660. Correlations that have t-values exceeding +1.660 or less than -
328   1.660 (two-tailed test) are significant (90% confidence).

329   **3   Results and Discussion**
330   **3.1 Meteorology and Atmospheric Circulation**
331   Knowledge of monthly (2009 to 2018) behavior of weather in the study region helps
332   interpretation of aerosol particle data. Philippine climate is influenced both by the winter
333   northeast monsoon (~November to April, Amihan) and the summer southwest monsoon (~May
334   to October, Habagat) (Coronas, 1920; Flores, 1969; Matsumoto et al., 2020). Median 3-hourly
335   temperatures at 975 mb per month (MERRA-2, 975 mb) (Fig. 1a) ranged from 23.2 °C in
336   January during the winter northeast monsoon, to 27.0 °C in May during the transition from the
337   summer season, as defined in (Bañares et al., 2021), to the southwest monsoon. May was also the
338   month with the lowest median 3-hourly relative humidity (76.6%) (MERRA-2, 975 mb) (Fig.
339   1b). The highest median level of relative humidity at 975 mb for a month was in August (86.5 %)
340   during the summer southwest monsoon, which is also the time of the year (June to August) when
341   rainfall peaks in the region where the sampling station (Manila Observatory) is located (Coronas,

342 1920; Cruz et al., 2013). The highest mean hourly precipitation (Fig. 1i) per month was from
343 July (0.46 mm hr^{-1}) to September (0.42 mm hr^{-1}), while March exhibited the lowest mean hourly
344 rainfall (0.02 mm hr^{-1}). Like relative humidity and precipitation, median precipitable water
345 (from available AERONET data of 513 points in August, 4015 points in February, and 5049
346 points in March) (Fig. 1h) was highest in August (4.9 cm) and lowest in February and March (3.1
347 cm and 3.2 cm, respectively).

348
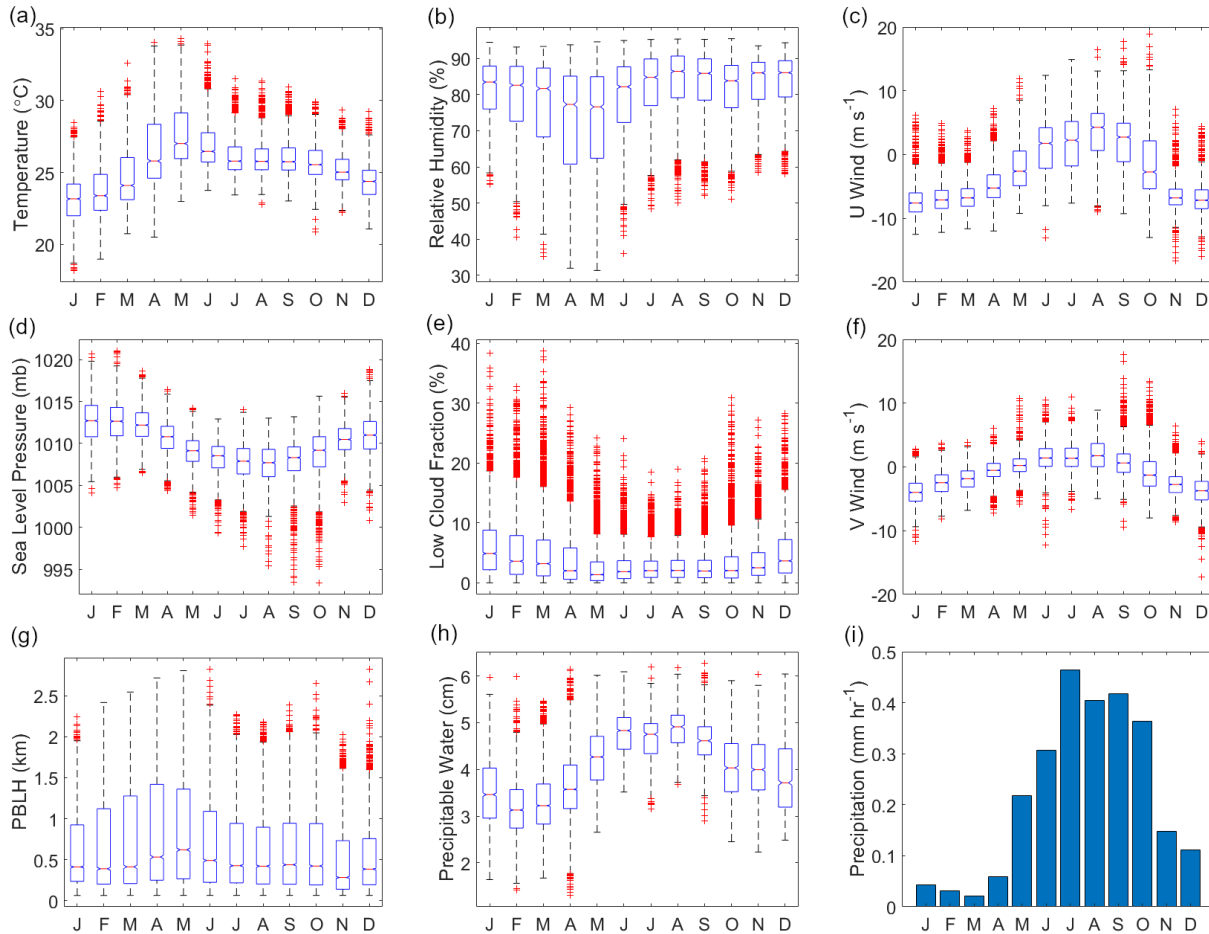
349

350

351 **Figure 1:** Monthly characteristics of meteorological parameters for Metro Manila, Philippines
352 based on data between January 2009 and October 2018. MERRA-2 parameters: (a) temperature
353 at 975 mb, (b) relative humidity at 975 mb, (c/f) u and v wind at 975 mb, (d) sea level pressure,
354 (g) planetary boundary layer height (PBLH), (e) low cloud fraction (cloud top pressure > 680
355 hPa); AERONET: (h) precipitable water (data counts per month Jan: 2131, Feb: 4015, Mar:
356 5049, Apr: 5844, May: 3448, Jun: 1696, Jul: 652, Aug: 513, Sep: 753, Oct: 1700, Nov: 2084,
357 Dec: 1449); PERSIANN: (i) mean hourly precipitation per month.

358

359 The lowest 3-hourly median pressures (MERRA-2) were observed (Fig. 1d) between July and
360 September during the southwest monsoon season (~985.2 – 985.8 mb). This is also the time
361 when the most number of tropical cyclones pass the island of Luzon (Wu and Choy, 2016). The

362   highest 3-hourly median pressures (988.1 – 990.0 mb) were during the winter northeast
363   monsoon.

364   Median winds (MERRA-2) were from the south/southwest direction from June to September
365   (Fig. 1c and 1f), associated with the summer southwesterly monsoon. HYSPLIT back-
366   trajectories show the same wind pattern (Fig. 2f to 2i). The highest median 3-hourly wind speeds
367   (MERRA-2) (Fig. 1c and 1f) during the southwest monsoon were recorded for August (u: 4.2 m
368   s^{-1} and v: 1.7 m s^{-1}). Median winds begin to transition in October and November (to the northeast
369   monsoon: Amihan) (Fig. 2j and 2k) coming from the east/northeast and maintained until
370   February (Fig. 2b), which is towards the end of the winter northeast monsoon. There were
371   generally higher wind speeds and the highest median 3-hourly wind speeds of the year
372   (MERRA-2) (Fig. 1c and 1d) in January (u: -7.6 m s^{-1} and v: -4.0 m s^{-1}). Median winds shifted
373   toward a more easterly source from March to May (transition time before the Habagat monsoon)
374   (Fig. 2c to 2e) accompanied by decreasing median 3-hourly wind speeds (u = -6.8 m s^{-1}, v = -1.9
375   m s^{-1} to u: -2.6 m s^{-1}, v = 0.2 m s^{-1}).
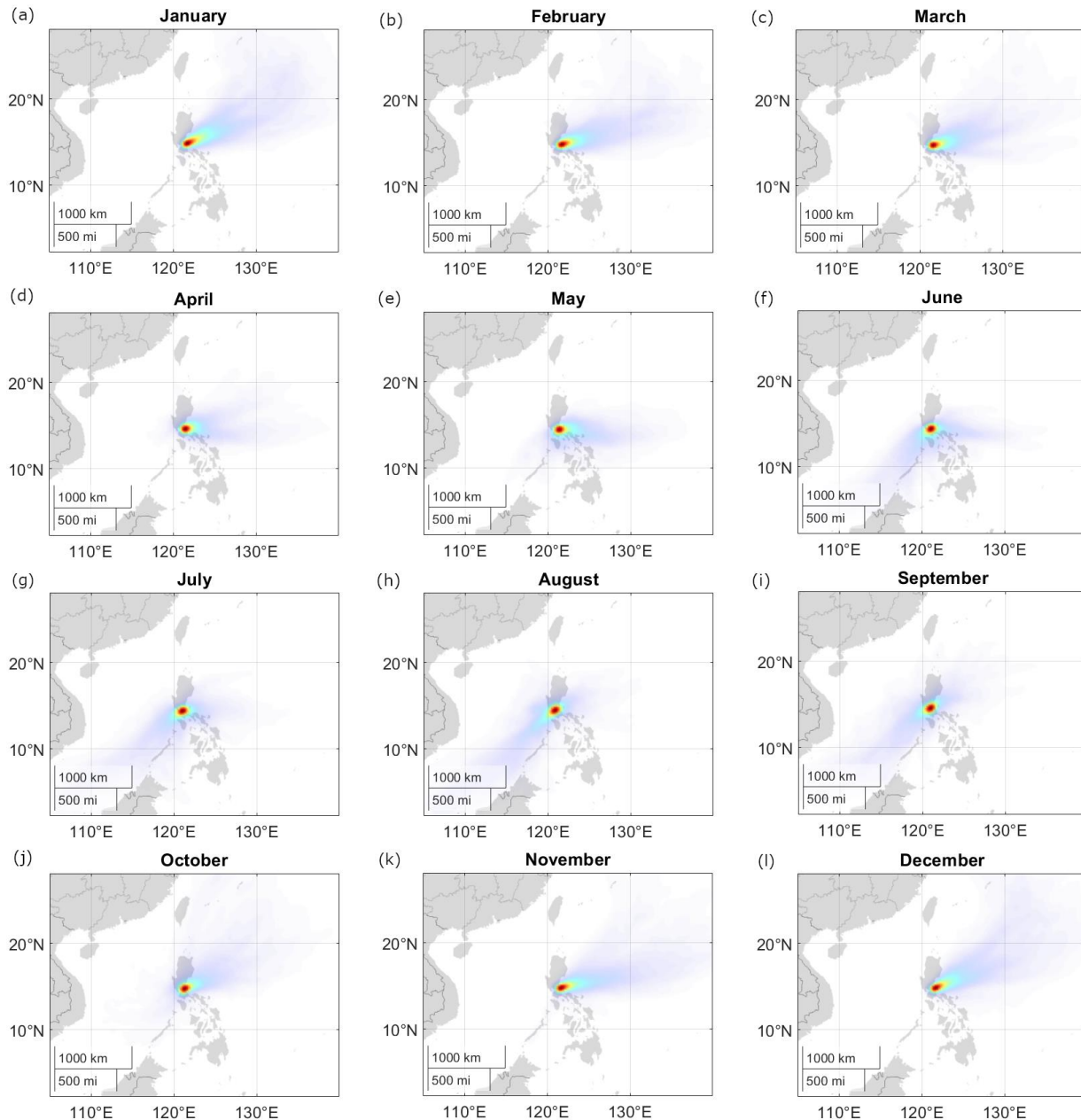
Figure 2: Density plots of HYSPLIT trajectories reaching Manila Observatory per month from 2009 to 2018. Red denotes areas with the greatest number of back trajectories within a 100 km radius. The colors represent density value contributions to Matlab-calculated cumulative probability distribution surfaces (100 km radius) from coordinates of three-day back trajectories of the specific months.

The transition times between the monsoons (when the wind directions shift and wind speeds change) are also the times of the highest (May, Fig. 1g, 621.2 m) and lowest (November, Fig. 1g, 279.6 m) median planetary boundary layer heights (MERRA-2). The median planetary boundary layer height was highest during the period (May) of highest temperatures, lowest relative humidity, reduced air pressure, and lowest monthly median low cloud fraction (MERRA-2) (Fig. 1e) (1.4 %). The lowest monthly median planetary boundary layer height was observed during

388   the period (November) when temperatures were beginning to cool and air pressure was rising.
389   The monthly maximum low cloud fraction was lowest in July (18.5 %) during the summer
390   southwest monsoon while the monthly median and monthly maximum low cloud fractions
391   (MERRA-2) (Fig. 1e) were highest (38.3 % max, 4.9 % median) in January during the winter
392   northeast monsoon.
393

394   **3.2 Aerosol Particle Characteristics**
395   3.2.1   Aerosol Optical Depth
396   Monthly median AOD (AERONET, 500 nm) (Fig. 3a) over the Manila Observatory was highest
397   from August (0.21) to October (0.23) around the time of the summer monsoon when winds were
398   coming from the southwest (Figs. 2h to 2i) (Holben et al., 2001). This is the same time of year
399   when biomass burning activities occur in the Indonesian region southwest of Metro Manila
400   (Glover and Jessup, 1998; Kiely et al., 2019; Cahyono et al., 2022). Studies have shown that
401   AOD in the Philippines increases during the biomass burning season in Indonesia (Nguyen et al.,
402   2019b; Caido et al., 2022). Regional AOD (550 nm) over the larger Southeast Asia domain from
403   MISR and MERRA-2 (Fig. 4) had a similarly large peak around the same time beginning in
404   September until October which, however, was second only in magnitude to a March peak, which
405   is influenced by biomass burning in Peninsular Southeast Asia (PSEA) (Gautam et al., 2013;
406   Hyer et al., 2013; Dong and Fu, 2015; Wang et al., 2015; Yang et al., 2022). This is consistent
407   with the peak in speciated AOD due to fine (radii <0.7 µm), spherical, and absorbing aerosols
408   that were observed by MISR from March to April (Fig. S1). This larger peak in March,
409   attributed to PSEA (which is ~2000 km west of the Philippines), was not as prevalent in the
410   AERONET AOD data over Manila Observatory in Metro Manila due to the dominant easterly
411   winds in the Philippines in March (Fig. 2c) and more localized sources.

412
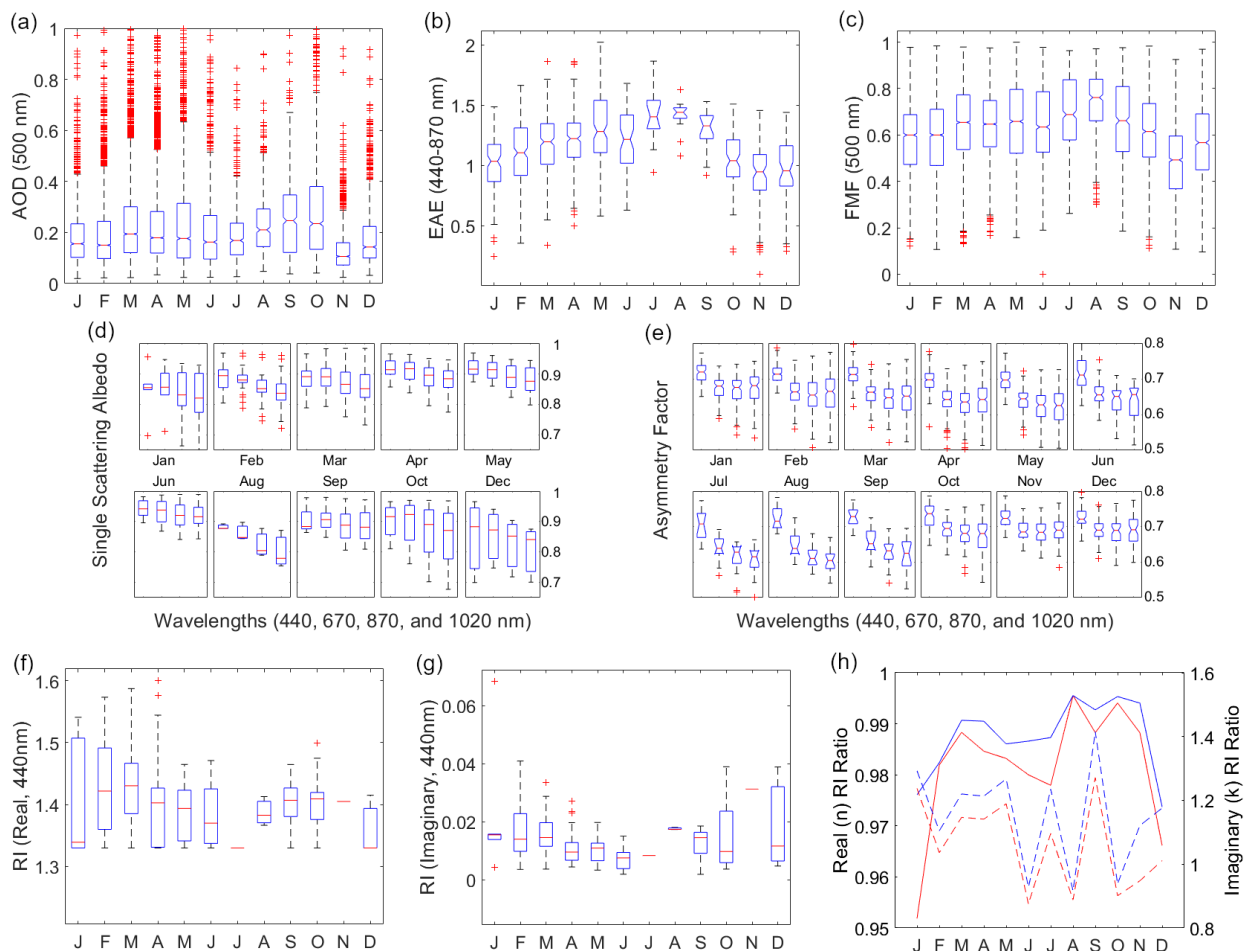
Figure 3: Monthly characteristics of AERONET aerosol particle parameters: (a) aerosol optical depth (AOD at 500 nm with y-axis until 1.0 only for larger boxplot resolution) with counts (Jan: 2107, Feb: 3931, Mar: 4923, Apr: 5755, May: 3389, Jun: 1653, Jul: 637, Aug: 483, Sep: 718, Oct: 1555, Nov: 2001, Dec: 1386), (b) extinction angstrom exponent (EAE at 440-870 nm) with counts (Jan: 102, Feb: 248, Mar: 312, Apr: 309, May: 137, Jun: 53, Jul: 14, Aug: 18, Sep: 18, Oct: 79, Nov: 77, Dec: 52), (c) spectral de-convolution algorithm (SDA) retrievals of fine mode fraction (FMF at 500 nm) with the same counts as AOD, (d) single scattering albedo (SSA) from 440 nm (leftmost boxplot) to 1020 nm (rightmost boxplot) with counts (Jan: 6, Feb: 31, Mar: 62, Apr: 50, May: 29, Jun: 8, Aug: 3, Sep: 5, Oct: 17, Dec: 3), (e) asymmetry factor (AF) from 440 nm (leftmost boxplot) to 1020 nm (rightmost boxplot) with the same counts as EAE, (f) real and (g) imaginary refractive index (RI) values (440 nm) with the same counts as SSA, and (h) refractive index ratios (where the blue line is the ratio of RI at 440 nm and 670 nm, the red line is the ratio of RI at 440 nm and the average RI for the 675–1020 nm wavelengths, and the broken lines are the imaginary refractive index ratios) for Metro Manila, Philippines based on data between January 2009 and October 2018.

There is a notable dip in the monthly median AERONET AOD over Manila Observatory from the peak in October to the lowest monthly median AOD (0.11) in November (Fig. 3a), just slightly above defined background levels (<0.1) (Holben et al., 2001), when the windspeeds were picking up and were coming from the east to northeast directions (Fig. 2k) in the direction of the Philippine Sea and the West Pacific Ocean. This dip was also observed in the regional

434 (30° × 30°) AOD data (MISR and MERRA-2, Fig. 4). This is most probably due to the decrease
435 in the AOD contribution from fine (radii <0.7 µm) and spherical particles based on size speciated
436 MISR AOD (Fig. S1). Larger and non-spherical particle contributions to AOD increase in
437 November in the Southeast Asia region. The MERRA-2 AOD is relatively higher than the MISR
438 AOD probably due to assimilation of MODIS data into MERRA-2. Studies in Asia (Xiao et al.,
439 2009; Qi et al., 2013; Choi et al., 2019) have observed relatively higher MODIS AOD compared
440 to MISR AOD.

441
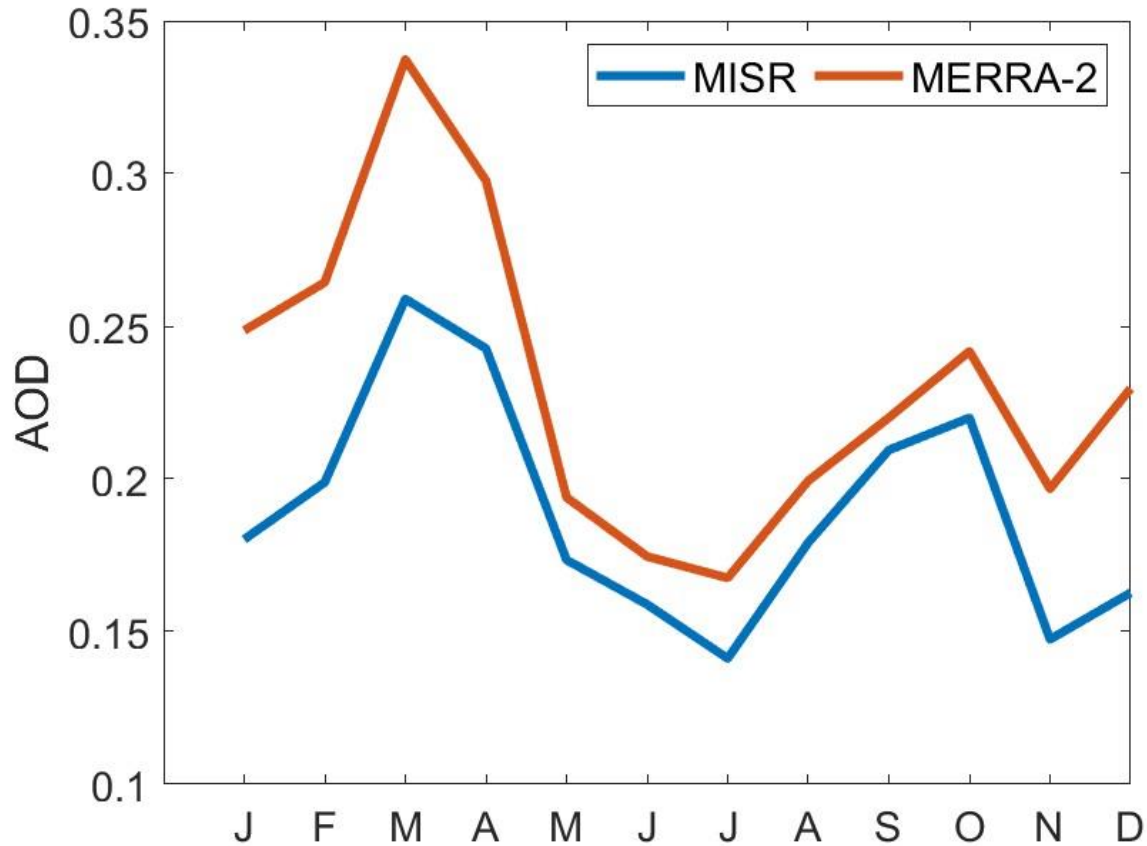
442

443 **Figure 4:** Monthly mean AOD (550 nm) in Southeast Asia (30° × 30°) from 2009 to 2018 from
444 MISR (blue line) and MERRA-2 (red line).

445 There were 338 instances (~1.2 % of the time based on the total number of 28,538 valid
446 AERONET AOD data points) of AOD values exceeding 1, indicative of heavy aerosol particle
447 loading (Huang et al., 2021). Because AOD is extrinsic (it depends on mass), AOD describes
448 total aerosol particle loading and we examine other aerosol particle parameters from AERONET
449 to make more informed inferences about size and composition.

450 3.2.2   Extinction Angstrom Exponent and Fine Mode Fraction

16

451   The extinction angstrom exponent (EAE) relates the extinction of light at specific wavelengths
452   and is indicative of aerosol particle size (Ångström, 1929). The EAE is usually greater for
453   smaller particles (~4 for very small particles that undergo Rayleigh scattering, > 2 for small
454   particles, < 1 for large particles like sea salt and dust, and 0 for particles as large as cloud drops)
455   (Schuster et al., 2006; Bergstrom et al., 2007). The highest monthly median EAE (Fig. 3b) from
456   2009 to 2018 over the Manila Observatory was observed from July (~1.4) to September (~1.3),
457   during the southwest monsoon. This period is associated with the biomass burning southwest of
458   the Philippines (Oanh et al., 2018; Stahl et al., 2021; Crosbie et al., 2022). The median (per
459   month) EAE ranged from ~0.9 in November to ~1.4 in August, a range which is within the
460   values from previous studies collected from mixed sites and urban/industrial areas with both fine
461   and coarse particles (Eck et al., 2005; Giles et al., 2012). The high EAE over Manila Observatory
462   from July to September is consistent with the regional (30° latitude x 30°longitude) MISR data
463   that shows increased AOD from fine, spherical, and absorptive particles (Fig. S1) in Southeast
464   Asia during the same months. This suggests that the high EAE observed at the Manila
465   Observatory during these months is not necessarily from local sources.

466   EAE increases with AOD (Fig. S2), which means that the greater particle loading is contributed
467   by smaller particles (Smirnov et al., 2002). Of the high loading cases (AOD >1) over Manila
468   Observatory, the EAE values were mostly greater than 0.8 indicating fine mode particles (Che et
469   al., 2015). The EAE values in August were the highest compared to other months including
470   having the highest minimum value of any month (0.71) (Fig. S2), due to smaller particles (~EAE
471   >1 for fine particles, Table 2). The lowest EAE values (0.08) and thus the largest particles were
472   observed in December, which again may be regional in nature with MISR EAE also lowest
473   during this time with increased AOD from larger and non-spherical particles (Fig. S1).

474   The fine mode fraction (FMF) describes the prevalence of fine mode particles in the column of
475   air above the surface. The fine mode fraction (Fig. 3c) from 2009 to 2018 was highest in August
476   (monthly median of 0.75) and lowest in November (monthly median of 0.45). This is consistent
477   with the EAE values discussed earlier with the prevalence of smaller particles in August and
478   larger particles in November. In August (Fig. 2h) the southwest monsoon is known to coincide
479   with the transporting of fine smoke particles to Luzon. In November (Fig. 2k), the prevalent
480   winds may have already shifted to easterly (Matsumoto et al., 2020) implying more marine-
481   related sources associated with coarser particles.

482   3.2.3   Single Scattering Albedo
483   The single scattering albedo (SSA) is the most important aerosol particle parameter determining
484   whether aerosol particles will have a warming or cooling effect (Reid et al., 1998). SSA is the
485   ratio of the scattering coefficient to the total extinction (scattering and absorption) coefficient
486   (Bohren and Clothiaux, 2006) of aerosol particles. Higher SSAs are related to more reflective
487   aerosol particles while more absorbing aerosol particles will have lower SSA values; values
488   range from 1 (reflective) to 0 (absorbing). Monthly median SSA values were largest in June
489   (0.94 at 440 nm), suggesting the presence of more reflective aerosol particles, and smallest in
490   August (0.88 at 440 nm and 0.78 at 1020 nm) suggesting more absorptive particles that are
491   similar in range to the SSA of biomass burning particles (Table 2). August is when biomass
492   burning is prevalent to the southwest of the Philippines and associated with soot particles that are
493   absorptive.

494 The sensitivity of SSA to different wavelengths depends on the type of aerosol particles present.
495 More specifically, aerosol particle size and refractive index (which is related to aerosol particle
496 composition) both affect the SSA (Dubovik and King, 2000; Bergstrom et al., 2007; Moosmüller
497 and Sorensen, 2018). For dust-type particles, SSA increases with wavelength because of lower
498 dust absorption in the higher visible to infrared wavelengths (Dubovik et al., 2002), while for
499 urban particles (including black carbon), which absorb light at longer wavelengths, SSA
500 decreases with wavelength (Reid et al., 1998; Bergstrom et al., 2002). The presence of organic
501 carbon may affect this spectral dependence; however, because organic particles absorb in the
502 UV, this lowers SSA at wavelengths shorter than 440 nm (Kirchstetter et al., 2004). Monthly
503 median SSA generally decreased with increasing wavelength for all months with available data
504 (Fig. 3d) presumably due to the influence of more urban particles in contrast to dust.
505 Noteworthy though are the monsoon transition months of April, September, and October (Fig.
506 3d), which had increased SSA from 440 nm to 670 nm, possibly from organics along with black
507 carbon due to transported smoke. The back-trajectories for these months (Figs. 2d, 2i, and 2j)
508 suggest sources from the northeast that are closer to Luzon during these months compared to
509 other months. This indicates the possibility of more local sources. Increasing the certainty of
510 sources associated with aerosol particles necessitates looking at other available aerosol particle
511 parameters, discussed subsequently.

512 3.2.4   Asymmetry Factor
513 The asymmetry factor quantifies the direction of scattering of light due to aerosol particles, with
514 values ranging from -1 (back scatter) to 0 (uniform scattering) to 1 (forward scatter). It is
515 important in modeling climate forcing because it affects the vertical distribution of the radiation
516 in the atmosphere (Kudo et al., 2016; Zhao et al., 2018). The asymmetry factor is dependent on
517 particle size, shape, and composition and the value of 0.7 is used in radiative models (Pandolfi et
518 al., 2018).

519 Lower asymmetry factors are related to smaller particles (at constant AOD) (Bi et al., 2014).
520 Measured values due to biomass burning, for example, are 0.54 (550 nm) in Brazil (Ross et al.,
521 1998) and 0.45 – 0.53 (550 nm and including dust) over central India (Jose et al., 2016). There
522 have been relatively higher values observed in western, central, and eastern Europe (0.57 – 0.61
523 at 520 – 550 nm) (Pandolfi et al., 2018) and the U.S. East Coast (0.7 at 550 nm) (Hartley and
524 Hobbs, 2001). In Norway, the asymmetry factor for background summer conditions was 0.62
525 and was higher in the springtime at 0.81 (862 nm) during Arctic haze events (Herber et al.,
526 2002). Highest values are associated with dust such as those measured in the Sahara being 0.72 –
527 0.73 (500 nm) (Formenti et al., 2000). Over Metro Manila, the asymmetry factors from the
528 AERONET data at the 675, 870, and 1020 nm were similar across months (Fig. 3e). The monthly
529 median asymmetry factors at 440 nm ranged from 0.70 (April and May) to 0.74 (October), while
530 for 670, 870, and 1020 nm the monthly median asymmetry factors were smaller and ranged from
531 0.62 – 0.69. These values were closely related to those observed over the U.S. East Coast as
532 mentioned earlier, perhaps due to the proximity of the location to the coast (10 km east of Manila
533 Bay and 100 km west of the Philippine Sea) as well as its location in Manila, which is a large
534 local source due mostly to vehicles (Cruz et al., 2019).

535 The monthly median asymmetry factor in Metro Manila was greatest towards the end of the year
536 (October to December) for all the wavelengths, suggesting larger particles when winds (Figs. 2j
537 to 2l) come from the Philippine Sea in the northeast. It was in March and April that the monthly

18

538   median asymmetry factor was minimal for 440 nm and in August for 670, 870, and 1020 nm.
539   These were the times when aerosol particles were smallest. March to April represents the driest
540   time of the year in Manila (Fig. 1b and 1h) perhaps preventing particle growth and where the
541   local sources may be dominating, even as back-trajectories (Fig. 2c and 2d) extend all the way
542   from the Philippine Sea to the east. This is corroborated by results from other studies showing
543   that the asymmetry factor seems to be enhanced by relative humidity (Zhao et al., 2018). The
544   unexpected low asymmetry factor values in August, however, are probably because of the source
545   of the particles. August had the highest relative humidity and precipitable water (Fig. 1b and 1h)
546   but is also when the back-trajectories (Fig. 2h) were from the southwest, possibly affected by the
547   Indonesia fires, which could have transported more non-hygroscopic fine particles.

548   Fine particles have been observed to exhibit decreasing asymmetry factors with increasing
549   wavelength (Bergstrom et al., 2003). This trend is observed in all the months for the monthly
550   median asymmetry factors (Fig. 3e) suggesting the predominance of smaller aerosol particles.
551   The greatest decrease in the asymmetry factor (all wavelengths) was in August, consistent with
552   the lowest observed values of the year (670, 870, and 1020 nm). Transported biomass burning
553   particles are the probable dominant particles during this time. They are usually composed of
554   hygroscopic inorganics, non-hygroscopic soot, and relative non-hygroscopic organic fractions
555   (Petters et al., 2009). Knowing the composition of biomass burning particles over the study
556   region will help in the understanding of hygroscopicity and its impacts on radiation.

557   3.2.5   Refractive Index
558   Refractive index is an intrinsic parameter as it does not depend on the mass or the size of
559   particles, and thus can be used to infer aerosol particle composition (Schuster et al., 2016). For
560   the case of the AERONET data, which include refractive index values that are insensitive to
561   coarse particles (Sinyuk et al., 2020), the focus of the discussion will be for fine mode particles
562   and may be limited when coarse particles are involved.   Refractive index measurements are
563   complex since they include real and imaginary parts related to light scattering and absorption,
564   respectively. All aerosol particles scatter light but only certain types absorb light significantly.
565   The most prominent particle absorbers in the atmosphere are soot carbon, brown carbon (organic
566   carbon that absorbs light), and free iron from dust (hematite and goethite in the ultraviolet to
567   mid-visible) (Schuster et al., 2016). For this study, we examine refractive index values at 440 nm
568   wavelength. Pure sources of soot carbon have the highest real refractive index values (~1.85) as
569   well as the highest imaginary refractive index (~0.71), both independent of wavelength (Koven
570   and Fung, 2006; Van Beelen et al., 2014). Brown carbon and dust have relatively lower real
571   refractive index values at 440 nm (~1.57 and ~1.54) and imaginary refractive index values
572   (~0.063 and ~0.008) that decrease with increasing wavelength (Xie et al., 2017).

573   In this study the range of the monthly median real refractive index values (440 nm) was from
574   1.33 (December and January) to 1.43 (March) (Fig. 3f). Water uptake by aerosol particles
575   decreases the real refractive index values (Xie et al., 2017) and thus the lowered real refractive
576   indices over the Manila Observatory can be due to the presence of more water in the atmosphere
577   in general and/or the increased presence of more hygroscopic particles. December and January
578   are not necessarily the months that have the highest moisture content, but they are months when
579   back-trajectories reaching the column over the Manila Observatory are from the Philippine Sea
580   to the northeast presumably transporting hygroscopic particles. As reported in previous sections,
581   relatively larger particles are observed around this time of the year and thus sea salt can be an

582   important contributor. The greatest change in the monthly median real refractive index with
583   increasing wavelength also was observed in December (Fig. 3h), possibly due the increased
584   fractional contribution of constituents other than soot carbon (because the real refractive index of
585   soot carbon is invariant with wavelength). Noteworthy as well is the month of August (Fig. 3f),
586   which has the smallest range of real refractive index values, possibly indicating a more
587   homogenous aerosol particle source compared to other months. August is the month with the
588   highest relative humidity (Fig. 1b) as well as highest precipitable water (Fig. 1h), while this is
589   also the month when long-range biomass burning emissions are observed to be highest, and
590   when the real refractive index values would otherwise be expected to be highest.

591   Water content seems to play a significant role in the real refractive index values in Manila.
592   March, when the monthly median real refractive index values are highest (Fig. 3f), is when
593   precipitable water vapor (Fig. 1h) is among the lowest in the year. The months around March are
594   also when maximum real refractive indices (1.57 in February, 1.59 in March, and 1.60 in April)
595   were observed (Fig. 3f). March was when there was a relatively small change in real refractive
596   index value with wavelength perhaps related to greater soot carbon fractions during this time,
597   due possibly to the contribution of biomass burning from Peninsular Southeast Asia (Shen et al.,
598   2014). Looking more closely at the imaginary refractive index values will help elucidate this
599   issue.

600   Monthly median imaginary refractive index values (440 nm) ranged from 0.007 in June to 0.015
601   in September and December (Fig. 3g). These are low compared to those of the pure soot carbon
602   mentioned earlier because of the mixed nature of the sampling site with contributions from
603   brown carbon and dust. The highest imaginary refractive index values in September and
604   December suggest the greatest fractional contribution of soot because the highest imaginary
605   refractive index values are associated with soot. These are also similar in magnitude to biomass
606   burning particles in the Amazon (0.013) (Guyon et al., 2003). The key distinction between soot
607   carbon and other major absorbers (brown carbon and dust) is that its imaginary refractive index
608   is invariant with wavelength. Both brown carbon and dust exhibit a decrease in the imaginary
609   refractive index with increasing wavelength (Xie et al., 2017). The ratios of imaginary refractive
610   index values (440 nm to average of 670–1020 nm) (Fig. 3h) show a relative invariance with
611   wavelength (ranging from 0.88 to 1.4), which indicates the dominance of soot as the major
612   absorber in the region (Eck et al., 2003). While observed wavelength invariance points to high
613   soot contributions, the size of the particles can help distinguish between brown carbon, which
614   reside mainly in the fine mode, and dust sources, which yield more coarse particles (Schuster et
615   al., 2016). September is during the southwest monsoon, which is when, as noted in the earlier
616   sections, fine particles were most prevalent. This is also the time when the imaginary refractive
617   index varied most with wavelength (1.4 ratio of the imaginary refractive index at 440 nm and the
618   imaginary refractive index average for 670 nm to 1020 nm in Fig. 3h) possibly with greater
619   absolute contributions from brown carbon, even with the highest soot carbon fractional
620   contributions. Brown carbon has been observed both from primary and aged aerosol particle
621   emissions from biomass burning (Saleh et al., 2013). As noted earlier, December also had the
622   highest imaginary refractive index values as well as relatively coarser particles, possibly due to
623   larger dust absolute contributions even with the highest soot carbon fraction contributions. The
624   lowest monthly median imaginary refractive index values in June, on the other hand, when fine
625   mode particles prevail suggest highest fractional contributions of brown carbon relative to other
626   months (Fig. 3h).

20

627   3.2.6   Volume Size Distributions
628   The volume size distribution (VSD) is another way to be able to more deeply characterize
629   aerosol particles, specifically related to their effect on climate, weather, and clouds (Haywood
630   and Boucher, 2000; Feingold, 2003). In the Manila Observatory dataset, there was a bi-modal
631   VSD for the entire dataset (Fig. 5a). The fine mode median values peaked in the accumulation
632   mode at 0.148 µm particle radius while the coarse mode median values peaked at 3.857 µm (Fig.
633   5a and Table S1). The median coarse mode amplitudes and volume concentrations were higher
634   than the fine mode amplitudes and volume concentrations for most of the year (DJF, MAM, and
635   SON, Fig. 5b and Table S1), except during the southwest monsoon (JJA) when the fine mode
636   amplitude and volume concentration was higher. This is consistent with observations earlier of
637   fine mode prevalence during the southwest monsoon. Median VSD amplitudes (Fig. 5c) were
638   greater in the afternoon, with higher peaks and volume concentrations for both the fine and
639   coarse modes, compared to the morning. There was a slightly larger coarse median amplitude
640   and volume concentration, compared to the accumulation mode median amplitude and volume
641   concentration, for both the morning and afternoon size distributions. While the VSDs confirm
642   several observations based on the analysis of the aerosol particle parameters presented earlier,
643   not much further information is gained especially regarding chemical composition. Size
644   distributions are a result of contributions from multiple sources, and thus being able to
645   discriminate the sources based on their characteristic size distributions will help identify relevant
646   sources.
647
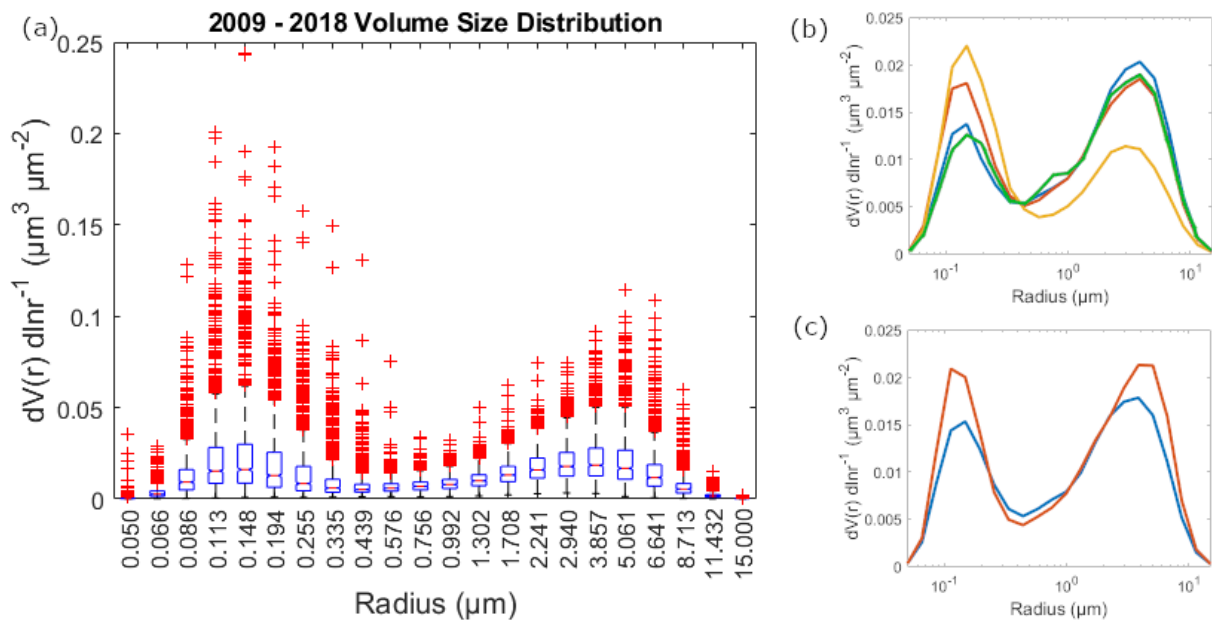
649   **Figure 5:** (a) VSD results derived from AERONET measurements at Metro Manila between
650   January 2009 and October 2018. Median VSDs over the study period based on (b) season (blue:
651   DJF, red: MAM, orange: JJA, green: SON) and (c) time of day (blue: AM, red: PM).
652
653   **3.3 Clusters**
654   3.3.1 VSD Cluster Profiles

655 Five clusters were identified to best represent the VSD (Fig. 6a). The average of the VSDs in
656 each cluster varied depending on the height of the peaks in the accumulation mode and the
657 coarse mode. In Metro Manila, the accumulation mode is associated with aged aerosol particles
658 and combustion (Cruz et al., 2019). The majority of the data (830 count out of 1419 total VSD
659 profiles) were clustered together in a profile (cluster 1) that had relatively low average
660 magnitudes of volume concentration for both the accumulation (0.01 $\mu m^3\ \mu m^{-2}$) and coarse (0.02
661 $\mu m^3\ \mu m^{-2}$) modes, with the volume concentration magnitude of the coarse mode peak slightly
662 higher than the volume concentration magnitude of the accumulation mode peak. The next
663 prevalent cluster profile (284 counts, cluster 2) had an average fine mode peak for the volume
664 concentration (0.04 $\mu m^3\ \mu m^{-2}$) which was more than twice as much than the previous profile but
665 with a similar coarse mode peak for the volume concentration (0.02 $\mu m^3\ \mu m^{-2}$). The average
666 coarse mode peak for the volume concentration (0.04 $\mu m^3\ \mu m^{-2}$) was the highest (compared to
667 the four other cluster profiles) for the third prevalent cluster profile (166 counts, cluster 3);
668 cluster 3 also had a slightly shifted volume concentration peak in the coarse mode to a higher
669 radius (5.06 μm) compared to other clusters. The coarse mode dominated this VSD compared to
670 other profiles (lower magnitude for the accumulation mode peak for the volume concentration,
671 0.02 $\mu m^3\ \mu m^{-2}$). The two remaining cluster profiles exhibited high average magnitudes of
672 volume concentration in both the accumulation and coarse modes. The fourth prevalent cluster
673 profile (74 counts, cluster 4) had the highest average absolute magnitude for the volume
674 concentration in the accumulation mode (0.11 $\mu m^3\ \mu m^{-2}$), while the fifth prevalent cluster profile
675 (65 counts, cluster 5) had a slightly smaller accumulation mode peak for the volume
676 concentration (0.07 $\mu m^3\ \mu m^{-2}$) that was shifted to a slightly higher radius (0.19 μm compared to
677 0.15 μm). Both clusters 4 and 5 had similar average coarse mode peak volume concentration
678 magnitudes (0.04 $\mu m^3\ \mu m^{-2}$).

679
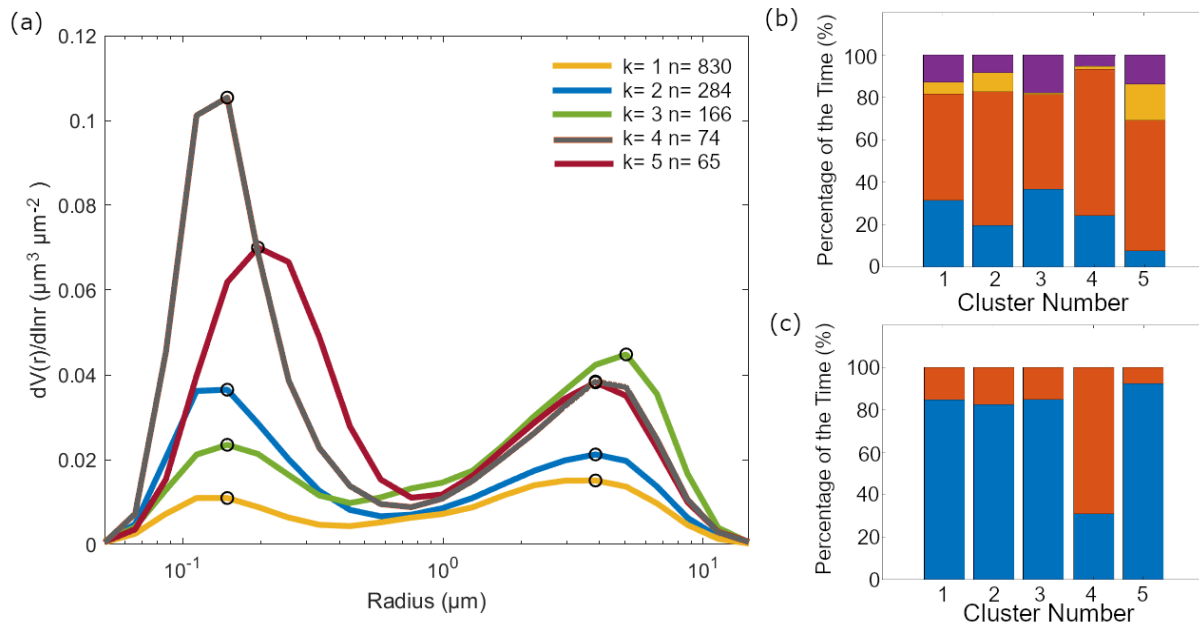
681 **Figure 6:** (a) Cluster analysis of VSD data yielding five characteristic and averaged VSDs with
682 the number of points per cluster shown in the legend. The black circles on the curves show the

22

683   peak locations in the submicrometer (<1 µm) and coarse (≥1 µm) modes. The relative abundance
684   of each cluster is shown for different (b) seasons (blue: DJF, red: MAM, orange: JJA, violet:
685   SON) and (c) times of day (blue: AM, red: PM).

686   The clusters were distributed across seasons (Fig. 6b), with clusters 1 and 2 being the most
687   evenly distributed among the clusters. Cluster 3, which had the highest coarse mode peak, had
688   the greatest contribution from September to November compared to other clusters. Cluster 4,
689   which had the highest accumulated mode peak compared to other clusters, had the greatest
690   contribution from March to May as well as to afternoon VSDs compared to other clusters (Fig.
691   6b and 6c). Relative contributions of VSDs from June to August were highest for cluster 5,
692   which had the shifted accumulated mode peak.

693   Median total (AERONET) AOD values (Fig. 7b) were lowest (0.12) for cluster 1, though it had
694   the second highest sea salt fractional contributions (31%) (Fig. 7a) to total AOD (MERRA-2)
695   among all the clusters. Cluster 2 had relatively mid-range median total AOD values (0.27) that,
696   along with clusters 4 and 5, were dominated by sulfate and organic carbon (46% and 20%).
697   Cluster 3 had similar, but slightly lower median total AOD (0.25) compared to cluster 2. Cluster
698   3 was distinct because it had the largest total (0.04) and fractional contribution (37%) from sea
699   salt among all clusters. Clusters 4 and 5 had the highest median total AOD values (0.47 and
700   0.56), with cluster 5 having the highest absolute and fractional sulfate contributions (0.14 and
701   64%) among the clusters. Integrating the above results with their corresponding aerosol particle
702   properties can help associate the clusters to air masses.

703
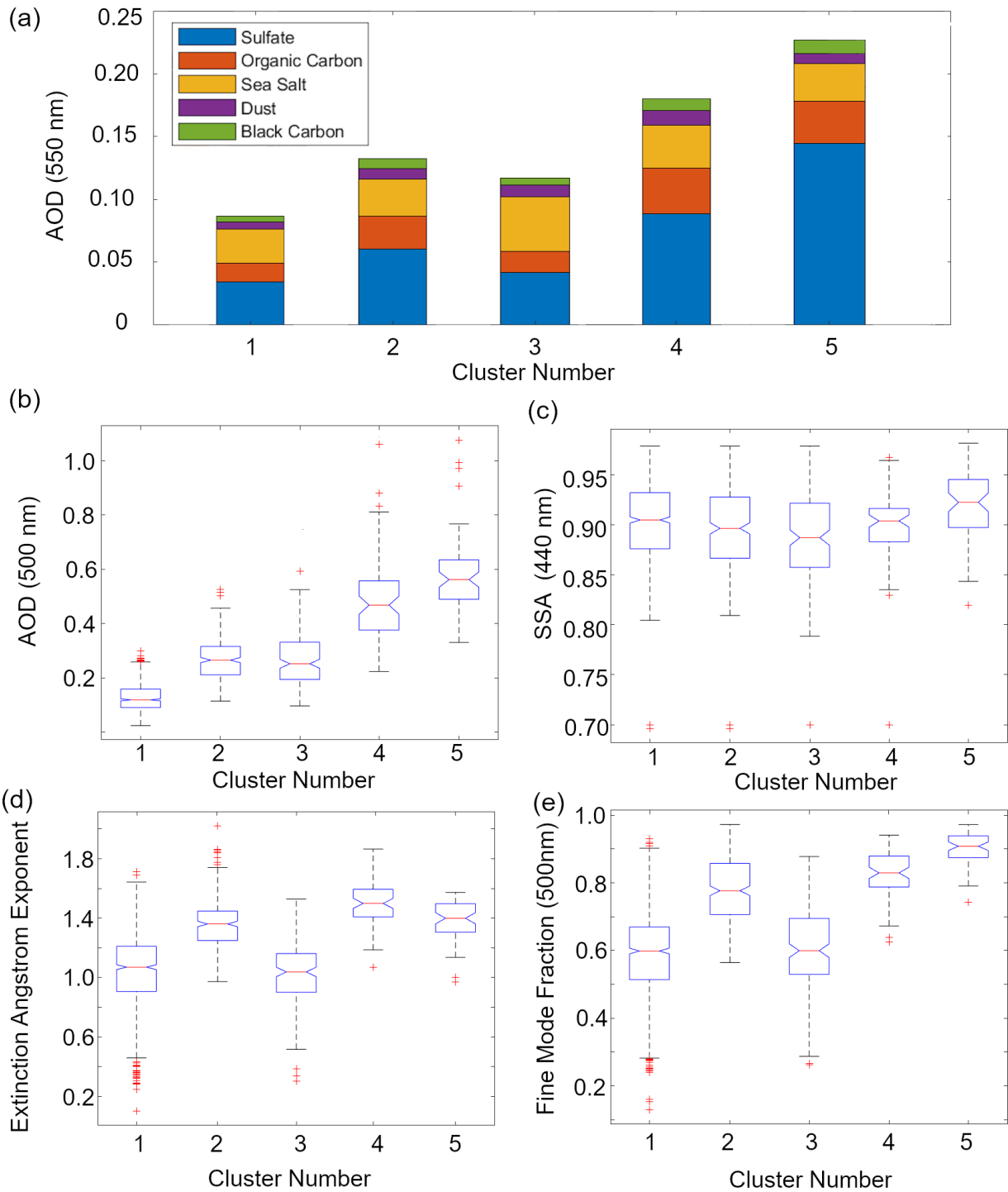
Figure 7: (a) Average compositional contributions to aerosol optical depth (AOD at 550 nm) from MERRA-2 per identified cluster (counts per cluster from 1 to 5: 830, 284, 166, 74, 65). Boxplots of AERONET (b) total AOD (500 nm), (c) single scattering albedo (SSA at 440 nm), (d) extinction angstrom exponent (EAE at 440 nm – 870 nm total), and (e) fine mode fraction (FMF at 500 nm) per cluster.

3.3.2 Air Mass Types

712 Air masses have been classified in previous studies based on their AOD, EAE, FMF, and SSA
713 values (e.g., Lee et al., 2010 and Aldhaif et al., 2021). The criteria from different studies (Table
714 2) were applied per cluster. The median total AOD of cluster 1 (0.12) was less than 0.2 (Fig. 7b),
715 which is the threshold for sea salt sources. Half of the data points in cluster 1 also fall below the
716 threshold for clean environments (AOD < 0.1) (Sorooshian et al., 2013). Based on its median
717 EAE (1.07, where EAE < 1 is coarse and EAE >1 is fine) and FMF (0.60) values (Fig. 7d and
718 7e), cluster 1 is a mixture of fine and coarse particles. The fine Cluster 1 is the only cluster with a
719 median that meets that threshold value for clean marine sources (AOD < 0.2), and we know from
720 Sect. 3.3.1 that its average VSD magnitude was greater for the coarse fraction and that its sea salt
721 contribution to total AOD was second greatest among the clusters. Thus, most probably, cluster 1
722 is a background clean marine source, since it also is predominant throughout the seasons (Fig.
723 6b). This makes sense given the proximity of the ocean to Metro Manila from both the east and
724 the west. The median SSA (0.90 at 440 nm) for cluster 1 (Fig. 7c), however, suggests the
725 presence of absorbing particles most probably due to high black carbon in the local source (Cruz
726 et al., 2019) that is mixed in with this generally clean marine source.

727 Most of the data from the other clusters all fall in the polluted category (Table 2), based on their
728 median total AODs (>0.1) (Fig. 7b). Cluster 2 has a median FMF value of 0.78 (Fig. 7e), which
729 suggests that most of the particles in this air mass are in the fine fraction. They are, however, not
730 sufficiently dominant in the aerosol for them to be typical of urban/industrial sources. The
731 average VSDs (Fig. 6a) of cluster 2 similarly suggest that their relative accumulation mode
732 magnitude is higher than the coarse magnitude, but not much higher. Like cluster 1, cluster 2 is
733 also more evenly distributed across the seasons (Fig. 6b). The median SSA for cluster 2 (0.90 at
734 440 nm) is also similar to the SSA of cluster 1 (Fig. 7c) where the local and background particles
735 are mixed. Cluster 2 could be a fine polluted background source superimposed on the dominant
736 marine source. Metro Manila is a megacity with continuous and large amounts of sources that
737 could be, due to its proximity to the ocean, interacting with the background.

738 Based on its median EAE value (1.04) (Fig. 7d), cluster 3 is mixed but mostly in the coarse
739 fraction, consistent with its VSD profile (Fig. 6a) which has the highest coarse magnitude (FMF
740 = 0.60) compared to the other clusters. The contribution of data from September to February is
741 greatest in cluster 3 (Fig. 6b), consistent with expected coarser particles during this period when
742 the winds are initially shifting from the southwest before becoming more northeasterly, as
743 previously noted. Median SSA (0.89 at 440 nm) was lowest for cluster 3 (Fig. 7c), this and the
744 relatively high coarse particle contribution suggests cluster 3 as a possible dust source based on
745 past studies (Lee et al., 2010). This air mass can be a mixture of local sources and transported
746 dust air masses. The large sea salt contribution (~37%) to total AOD in cluster 3 (Sect. 3.3.1) can
747 be related to long-range transport.

748 Both clusters 4 and 5 have median total FMF (0.83 and 0.91) (Fig. 7e) values exceeding the mark
749 (> 0.8, Table 2) for urban/industrial air masses. Combining this and results from the previous
750 sections confirms that cluster 4 can be an urban/industrial source given that it had the highest
751 median accumulated mode peak and organic carbon contribution (~20%) to total AOD among
752 the clusters. The median SSA for cluster 4 (0.90 at 440 nm) was similar to the median SSA of
753 clusters 1 and 2 (Fig. 7c), but the maximum SSA value for this cluster was lowest in general
754 among all the clusters suggesting cluster 4 has the net most absorptive effect. The cluster 4 air
755 mass is probably from local sources and transported biomass burning emissions. The high

756 median EAE (1.40, Fig. 7d) may be associated with aerosol particles due to biomass burning
757 (Deep et al., 2021).

758 Cluster 5 had the highest median total AOD (0.56) and FMF (0.91) values (Fig. 7b and 7e). It
759 also had the highest sulfate contribution (~64%) to total AOD (Fig. 7a), the highest median SSA
760 (0.92 at 440 nm, thus most reflective particles among the clusters) (Fig. 7c), and a shifted
761 accumulation mode peak (Fig. 6a). These characteristics suggest that cluster 5 is a possible cloud
762 processing air mass (Eck et al., 2012). The larger peak in the accumulation mode is possibly the
763 cloud signature. Previous studies have attributed this larger mode to cloud processing due to the
764 conversion of SO_2 to sulfate (Hoppel et al., 1994). Cloud processing is a major source of sulfate
765 (Barth et al., 2000).

766 The distribution of the air masses based on the abundance of the VSD profiles per cluster suggest
767 prevalent clean marine (58% of the total VSD counts) and background fine polluted (20%) air
768 masses over Metro Manila. The mixed dust (12%), urban/industrial (5%), and cloud processing
769 (5%) air masses contribute 22% altogether. We can investigate more deeply and look at specific
770 case studies that can better describe the air masses identified here.
771
772 **3.4   Case Studies**
773 Selected case studies are used to highlight periods with the highest AOD values and strongest
774 clear sky (no rain and heavy clouds) daytime aerosol particle sources within the sampling period.
775 As such, the clusters that are associated with the selected case studies are the clusters (3-5) with
776 higher VSD concentration magnitudes.
777
778 3.4.1   Long Range Transport of Smoke
779 Both cases of long-range transport of smoke discussed below have similar VSDs (Fig. 8a and 9a)
780 to the urban/industrial cluster VSD (cluster 4, Fig. 6a). Organic carbon was the dominant
781 contributor to AOD (Fig. 8b and 9b) for both long-range transport cases. The first of two events
782 occurred around 1 April 2020 with smoke presumed to come from East Asia. The VSD of this
783 specific case (Fig. 8a) is most like the urban/industrial cluster (cluster 4 in 3.3.2, Fig. 6a) because
784 of the high magnitude of its accumulated mode peak, its timing (April), and the enhanced
785 organic carbon contribution to AOD in the area (Fig. 8b). Though the absolute black carbon
786 contribution to AOD was highest here compared to the other case studies, and in general for the
787 AERONET data, it was organic carbon that was more prevalent in terms of contribution to total
788 AOD. Smoke is comprised of both soot carbon and organic carbon, amongst other constituents
789 (Reid et al., 2005).
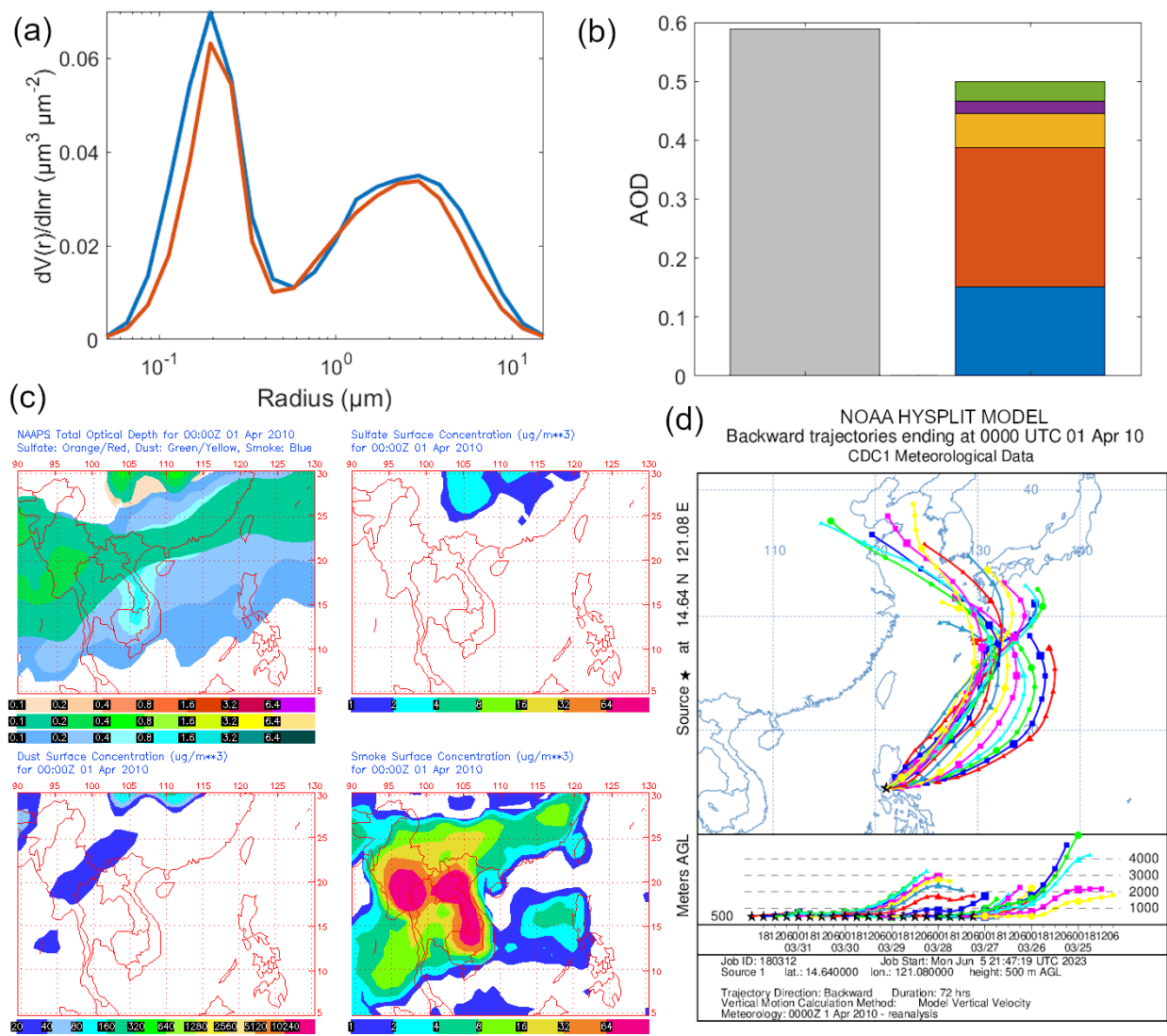
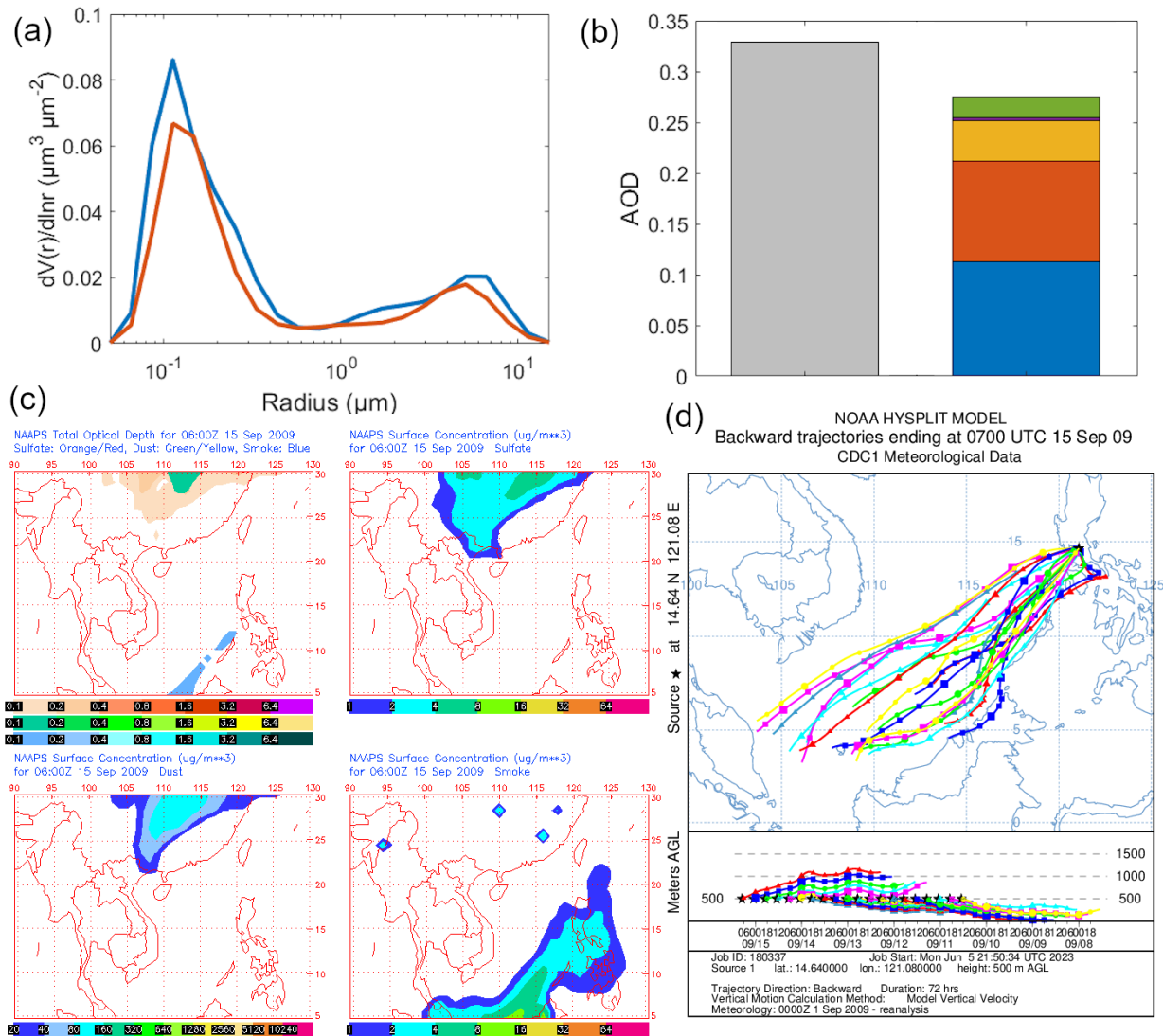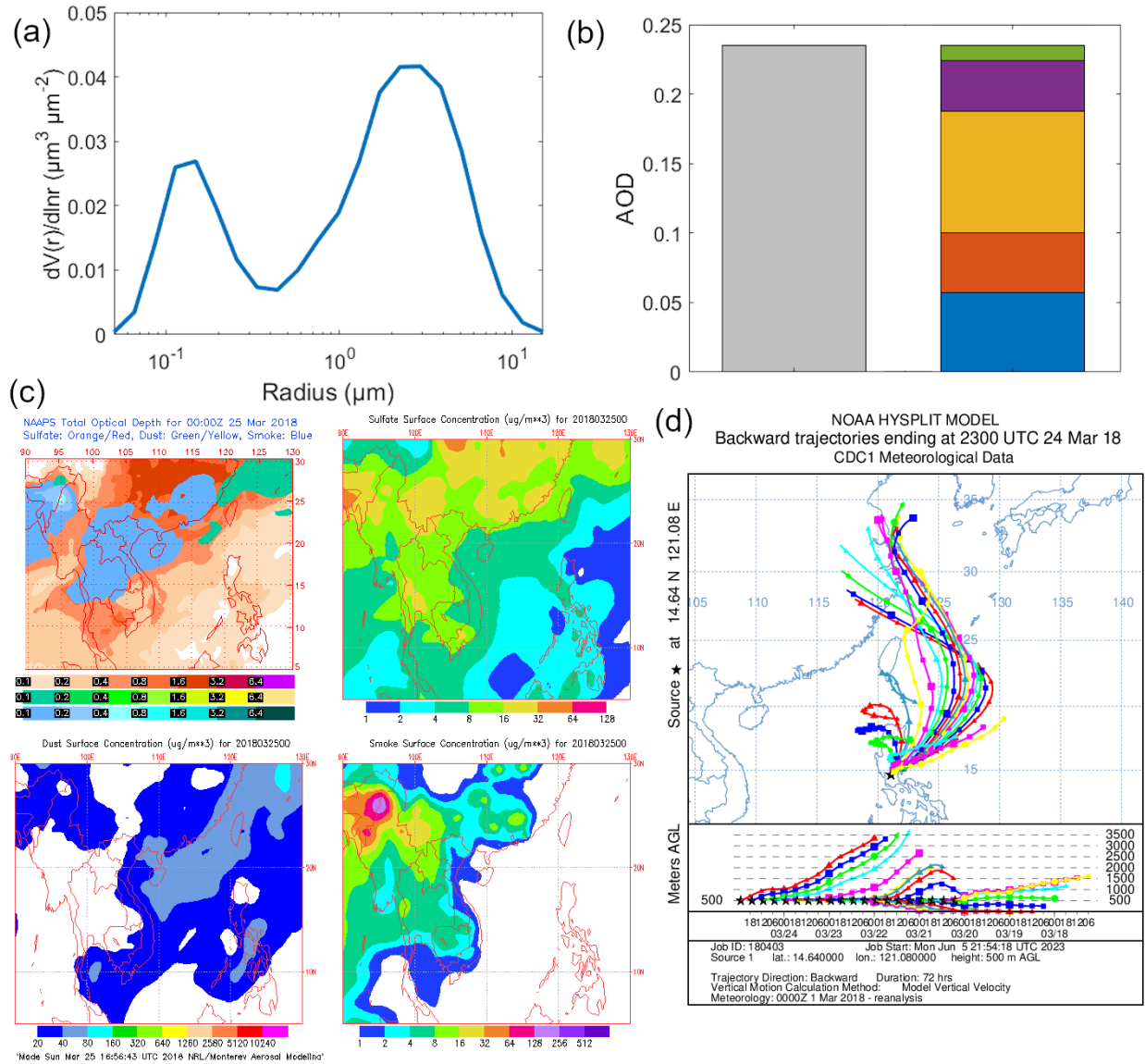**Figure 8:** Case study of long-range transport (smoke – East Asia) around 1 April 2010. (a) AERONET VSDs at (blue) 00:01 and (red) 00:26 UTC, (b) AOD from AERONET (gray: median AOD at 500 nm) and MERRA-2 hourly (green: black carbon, violet: dust, yellow: sea salt, orange: organic carbon, blue: sulfate) compositional contributions to AOD (550 nm) closest in time to 00:01 UTC, (c) NAAPS maps of total and compositional hourly AOD (orange/red: sulfate, green/yellow: dust, blue: smoke) and sulfate, dust, and smoke surface concentrations at 00:00 UTC, and (d) HYSPLIT seven-day back-trajectories arriving at Manila Observatory at 00:00 UTC.

The smoke contribution to AOD from NAAPS (Fig. 8c) for the first smoke case was visible in the Philippines (0.2) and seemed to come from East Asia where the smoke contribution to AOD was greater (reaching 0.8) especially in Peninsular Southeast Asia. Smoke surface concentrations were also widespread (Fig. 8c) with greatest concentrations in East Asia that reached the Western Philippines, though seemingly disconnected over the sea. There were observed biomass burning emissions in the Peninsular Southeast Asia (southern China, Burma, and Thailand) at

805   this time (Shen et al., 2014). The direction of the air mass coming into Metro Manila was from
806   the northeast, which curved from the west in the direction of East Asia based on HYSPLIT back-
807   trajectories (Fig. 8d).

808   The second smoke case was on 15 September 2009 with the source being Southeast Asia. The
809   back-trajectories of this case study (Fig. 9d) are from the southwest of the Philippines, and in the
810   direction of the Malaysia and Indonesia. NAAPS maps likewise show elevated AOD,
811   specifically smoke contribution to AOD (Fig. 9c), as well as enhanced smoke surface
812   contributions in the area around Metro Manila for this second smoke case study. The observed
813   AOD and smoke surface concentration increased specifically from the southwest of the
814   Philippines in the same direction of the back-trajectories. There were fires in the lowland (peat)
815   forests of Borneo around this time (NASA, 2009). MERRA-2 AOD contributions for this case
816   were greatest due to organic carbon as well as sulfate (Fig. 9b), and the absolute black carbon
817   contributions were greatest compared to other cases. The VSD of this smoke case from Southeast
818   Asia (Fig. 9a) resembled that from long-range transported smoke from East Asia (Fig. 8a) and
819   the urban/industrial air mass (cluster 4, Fig. 6a). This case occurred in the afternoon, which was
820   the prevalent time that the urban/industrial air mass was observed (Fig. 6c).

Figure 9: Case study of long-range transport (smoke – Southeast Asia) around 15 September 2009. (a) AERONET VSDs at (blue) 07:27 and (red) 07:52 UTC, (b) AOD from AERONET (gray: median AOD at 500 nm) and MERRA-2 hourly (green: black carbon, violet: dust, yellow: sea salt, orange: organic carbon, blue: sulfate) compositional contributions to AOD (550 nm) closest in time to 07:27 UTC, (c) NAAPS maps of total and compositional hourly AOD (orange/red: sulfate, green/yellow: dust, blue: smoke) and sulfate, dust, and smoke surface concentrations at 06:00 UTC, and (d) HYSPLIT seven-day back-trajectories arriving at Manila Observatory at 07:00 UTC.

3.4.2   Long Range Transport of Dust

The VSD of this specific case on 24 March 2018 (Fig. 10a) was most similar to the mixed dust cluster (cluster 3), which had a mixed size distribution but a more dominant coarse contribution. This is consistent with the most dominant contribution to AOD in the area, which was sea salt and dust (Fig. 10b). The back-trajectories were from East Asia around the same latitude as Taiwan (Fig. 10d). That area, at that time, had increased AOD in general from sulfate and dust

(Fig. 10c). The AOD from both AERONET and MERRA-2 (Fig. 10b) are lower than 0.3 (the AOD threshold for dust in other studies, Table 2) because of the long distance from the source (thousands of kilometers). The dust and sulfate seemed to have been transported to Metro Manila from East Asia based on the NAAPS sulfate and dust surface concentrations (Fig. 10c).

Figure 10: Case study of long-range transport (dust) around 24-25 March 2018. (a) AERONET VSD at (blue) 23:23 UTC, (b) AOD from AERONET (gray: AOD at 500 nm) and MERRA-2 hourly (green: black carbon, violet: dust, yellow: sea salt, orange: organic carbon, blue: sulfate) compositional contributions to AOD (550 nm) closest in time to 23:23 UTC, (c) NAAPS maps of total and compositional hourly AOD (orange/red: sulfate, green/yellow: dust, blue: smoke) and sulfate, dust, and smoke surface concentrations at 00:00 UTC on March 25, and (d) HYSPLIT seven-day back-trajectories arriving at Manila Observatory at 23:00 UTC.

3.4.3   Cloud Processing

852   Sulfate dominated the AOD (Fig. 11b) for this case on 26 August 2009 in the area around Metro
853   Manila. This along with its VSD exhibiting a second peak (Fig. 11a) in the accumulation mode
854   make it very similar to the cloud processing cluster (cluster 5). Sulfate has been known to be
855   enhanced through chemical productions in clouds and is used as a signature for cloud processing
856   (Barth et al., 2000; Ervens et al., 2018). Aqueous production of sulfate is significant in areas with
857   sources and clouds (Barth et al., 2000), and this case study has both. Aside from the high sulfate
858   contribution to AOD, the cloud fraction (Aqua/MODIS, Terra/MODIS, Fig. S3) is very high
859   (~100%) in the area of the back-trajectories (Fig. 11d). Interestingly, there is no regional AOD
860   elevation observed in the NAAPS maps (Fig. 11c) for this time. There are increased surface
861   smoke and sulfate levels in East Asia as well as southwest of the Philippines, and though the
862   back-trajectories do show a northeastward direction, they do not reach far enough into mainland
863   East Asia. It is possible that even while there are known regional sources of sulfate in Southeast
864   Asia (Smith et al., 2011; Li et al., 2017), this case could be local to the Philippines. There is in
865   fact a large power plant northwest of Metro Manila (Jamora et al., 2020).
866

867
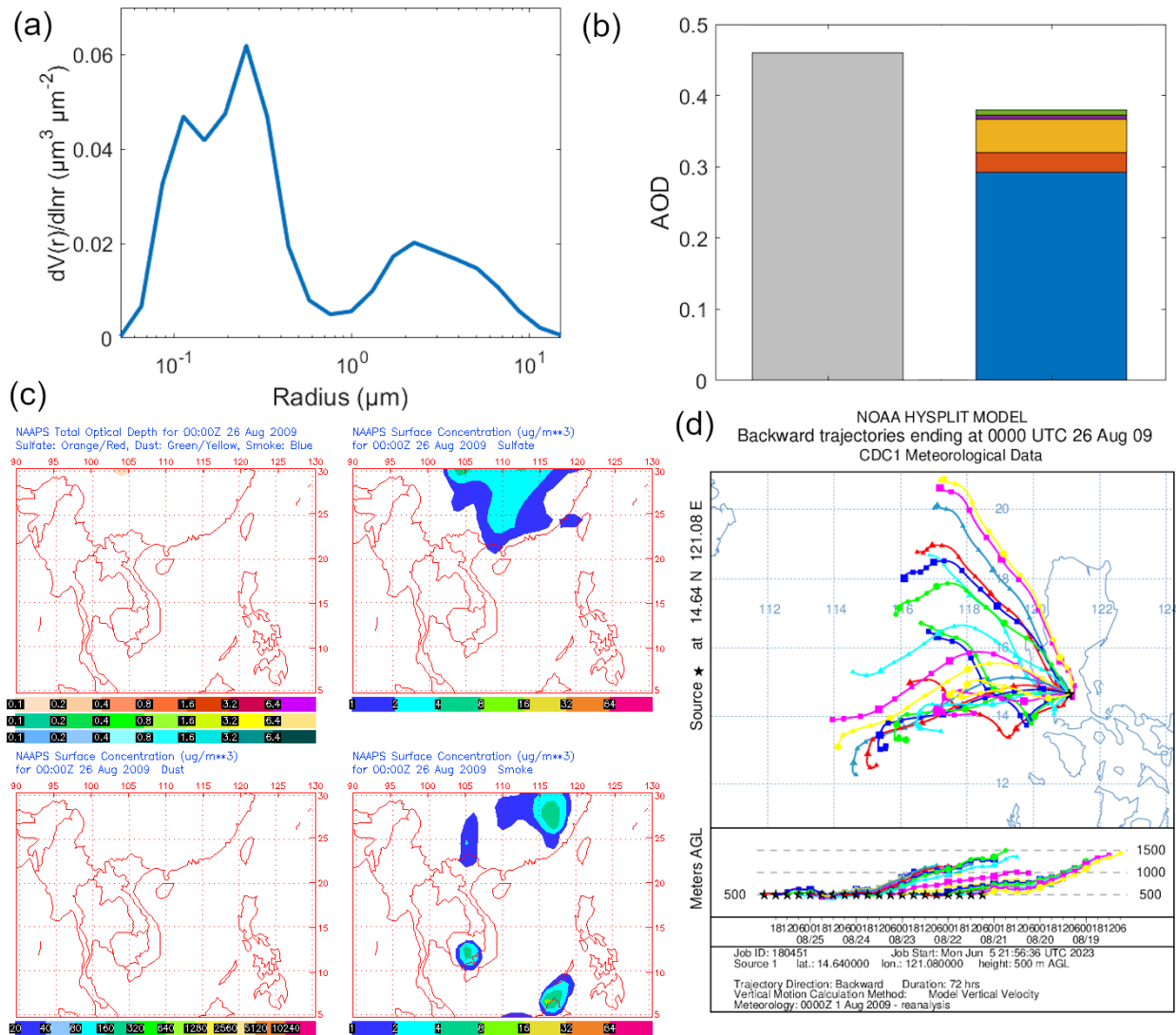
Figure 11: Case study of cloud processing on 26 August 2009. (a) AERONET VSDs at 00:18
UTC, (b) AOD from AERONET (gray: median AOD at 500 nm) and MERRA-2 hourly (green:
black carbon, violet: dust, yellow: sea salt, orange: organic carbon, blue: sulfate) compositional
contributions to AOD (550 nm) closest in time to 00:18 UTC, (c) NAAPS maps of total and
compositional hourly AOD and contributions and smoke surface concentrations at 00:00 UTC,
and (d) HYSPLIT seven-day back-trajectories arriving at Manila Observatory at 00:00 UTC.

3.5   EOF Analysis of AOD in Southeast Asia

The air masses in Metro Manila are influenced by regional sources which were identified
through EOF analysis of AOD. Three principal components (PC, Fig. 12) explained most of the
data variance (73.77%) (Fig. 12a) and were all well-separated from each other and are therefore
most probably the major distinct aerosol particle sources in the region. They will be the focus of
the subsequent discussion.

32
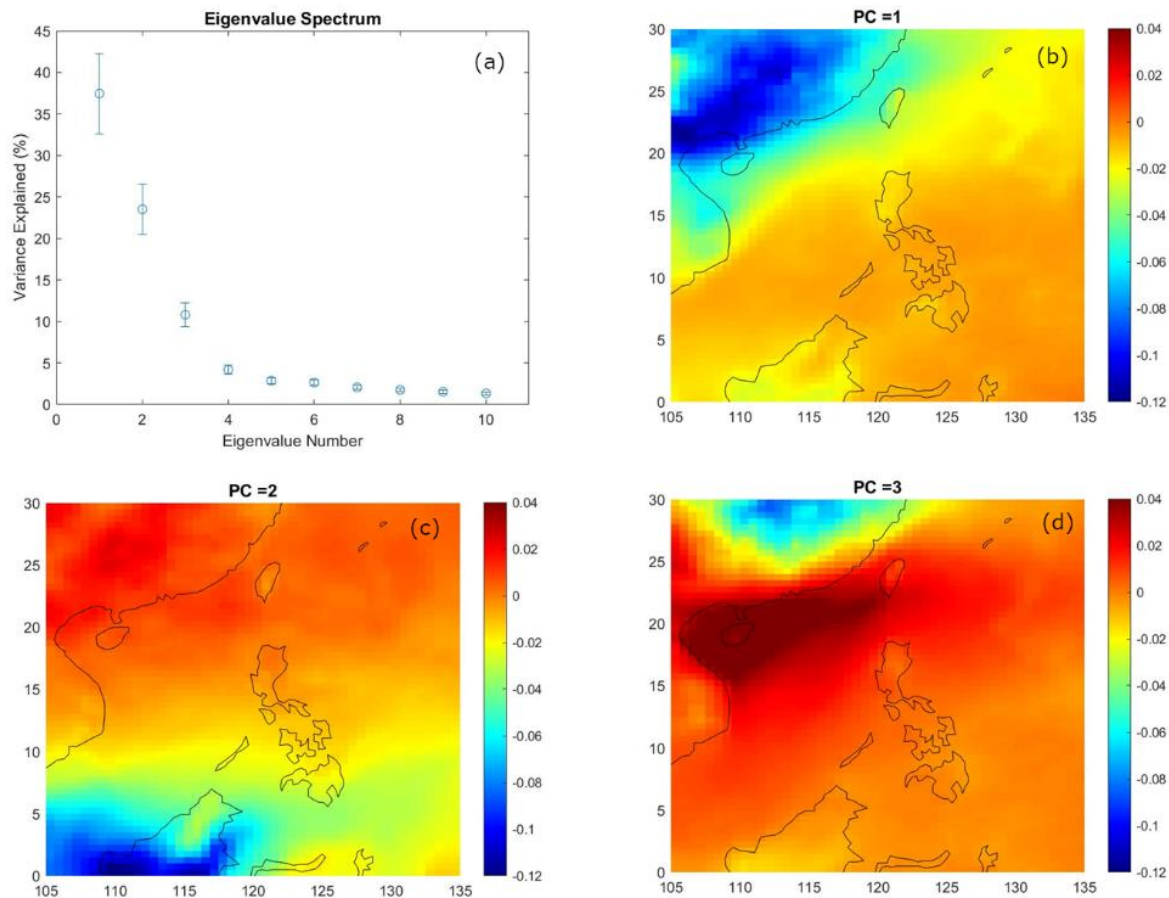
Figure 12: Results of the singular value decomposition. (a) Eigenvalue spectrum of the first ten eigenvalues, (b-d) maps of the coefficients of regression AOD anomalies onto the first three principal components.

The first PC explains 37.46% of the data variance (Fig. 12a) and, based on the map of the regression coefficients (Fig. 12b), separates mainland East Asia from the Philippines and Indonesia. East Asia is a globally recognized source for high AOD (Li et al., 2013), and its contribution to particles in Southeast Asia possibly corresponds to the first PC. The second PC explains 25.51% of the data variance (Fig. 12a) and separates southern Southeast Asia from northern Southeast Asia at around 15° N (Fig. 12c). Southern Southeast Asia is a known regional source of aerosol particles due to biomass burning (Cohen et al., 2017) and could be associated with the second PC. The third PC explains 10.80% of the data variance (Fig. 12a) and separates northern East Asia from southern East Asia mainland and the rest of Southeast Asia (Fig. 12d).

To gain confidence in the association of the PCs with their sources, we present correlation maps between the first three PCs to the fractional contributions of sulfate and organic carbon to AOD for the entire dataset.

The correlation maps of the first PC and the sulfate contribution to AOD (Fig. 13a and 13d) show high and statistically significant correlations (gray areas) in mainland East Asia and Taiwan, parts of western Philippines and Borneo, which are the probable sulfate sources. Clues from the mean monthly wind vector maps in April (Fig. 14a and 14d) and mean monthly AOD in

33

902 either March or April (Fig. S4c or S4e) most resembling the features of regression map of the
903 first PC (Fig. 12b) and the PC time series peaking in March (Fig. S5) together suggest that the
904 first PC may be associated with air masses that are present around March or April. Emissions
905 sources and meteorology that are dominant during the peak dates in the PC time series offer
906 clues to the attribution of each PC. The Southeast Asia region and the Philippines is influenced
907 by the monsoon systems (Coronas, 1920; Matsumoto et al., 2020) and February to March is the
908 time when the winds are transitioning from the northeasterly to easterly. The first PC could be
909 affected by the easterly winds, which are dominant around March when its PC values peaked.
910 The higher-level winds (free troposphere) (Fig. 14a) in April are from the west in mainland East
911 Asia and are from the east in the Philippines and it is possible that the different wind regimes are
912 distinguishing the sulfate sources in East Asia and the Philippines and beyond. Sulfate is a
913 known product of industry in East Asia (Smith et al., 2011; Li et al., 2017) while the West Luzon
914 and West Visayas islands have large power plants (Jamora et al., 2020).
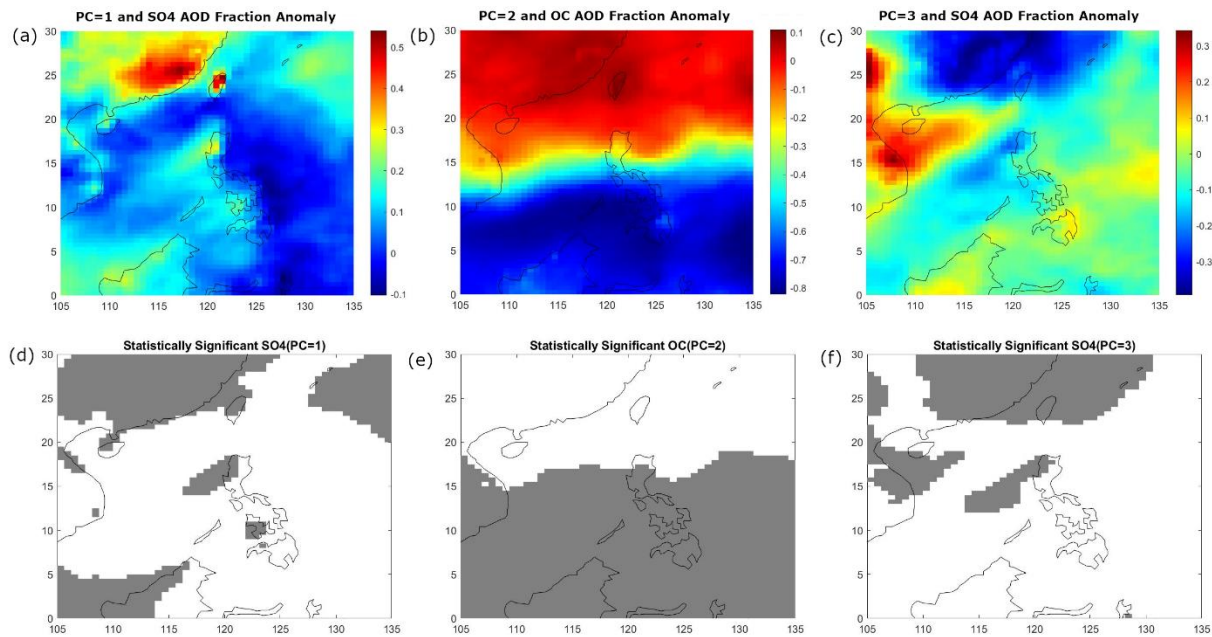
915
916 **Figure 13:** Correlation coefficients of principal components with (a/c) sulfate AOD fraction and
917 (b) organic carbon AOD fraction. Statistically significant (90%, d-f) areas are shaded gray.

34
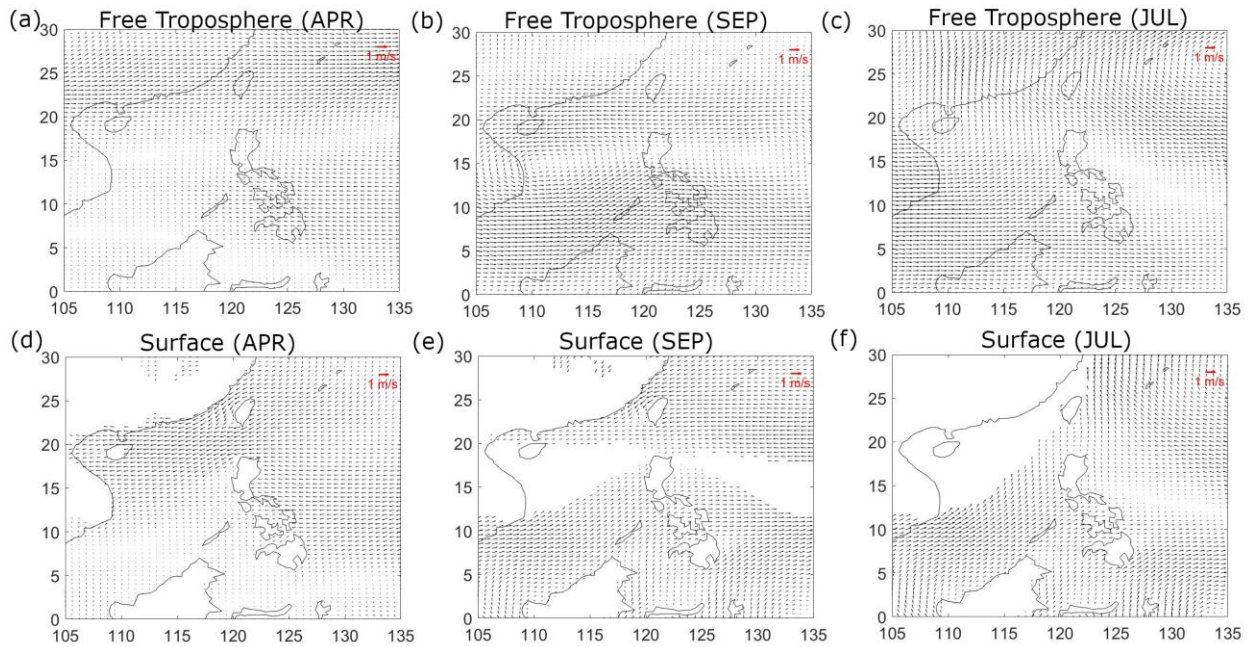
Figure 14: Monthly averaged winds for (a & d) April, (b & e) September, and (c & f) July from
MERRA-2 at (725 hPa, a-c) the free troposphere approximate and at (1000 hPa, d-f) the surface.

The correlation maps of the second PC and the OC contribution to AOD (Fig. 13b and 13e) show
high and statistically significant correlations from 0° to 15° N. The large magnitude of the
correlation coefficient (gray areas in Fig. 13b) stands out in southern Southeast Asia and is the
potential OC source. In this case, it is known that Indonesia is a major source of biomass burning
during its fire season (Glover and Jessup, 1998), and thus the local significance established in the
southern Southeast Asia is most likely due to the Indonesia biomass burning source. The burning
season in Indonesia is from August to October, and that is the same time when the AOD values
peak in the area (Fig. S4h, S4i, and S4j), as well as the peak of the second PC in the time series
(Fig. S5). Winds are usually from the southwest and west due to the southwest monsoon from
September to October, when the second PC peaked, and thus the second PC may be related to the
southwest monsoon. During the same time the surface and free troposphere mean monthly winds
(Fig. 14b and 14e) are from the southwest (in the general direction of Indonesia) towards the
south portion of Southeast Asia and thus corroborate the observation that the second PC may be
highlighting the regional effect of the Indonesia forest fires. Of interest is the line of separation
of the northern and southern Southeast Asia in the principal component that is within the area of
the monsoon trough (Wang et al., 2007). This line is also evident in the surface and the free
troposphere maps where the southwest winds from the area of Indonesia meet the easterlies in
north Southeast Asia (Fig. 14b and 14e) and which thus appears to be limiting the dispersion of
the biomass burning emissions to southern Southeast Asia.

The third PC was also well correlated to the sulfate AOD fraction though, compared to the first
PC correlation maps, there were distinctions between the northern and southern East Asia
regions (Fig. 13c and 13f). The local Philippine source still came out in the correlation maps as a
significant source. It was not clear from the PC time series (Fig. S5), which showed peaks in the
third PC in February, how the dates were related to the PC profile. The free troposphere winds in
July (Fig. 14c), as well as the AOD monthly mean map in July (Fig. 14c), however, showed

35

946 more similarities to the third PC regression map. Both showed a delineation between the
947 northern East Asia and southern East Asia (including Hong Kong) features. Mean winds (Fig.
948 14c) in the free troposphere are from the west, due to the southwest monsoon, in the area around
949 the Philippines, and they were from the northeast in north Southeast Asia. The interface of the
950 winds is within the approximate location of the monsoon trough in July (Wang et al., 2007), and
951 it is thus possible that the monsoon trough is causing the separation of the sulfate sources. This
952 could be investigated further. The monsoon trough has been noted to scavenge aerosol particles
953 from southern Southeast Asia (Reid et al., 2013). It is evident from the analysis that meteorology
954 affects the transport and processing of aerosol particles in region which along with local sources
955 contribute to the aerosol composition in Southeast Asia (Cruz et al., 2019; AzadiAghdam et al.,
956 2019; Braun et al., 2020; Hilario et al., 2020b; Hilario et al., 2022).
957
958 **4. Conclusion**

959 Metro Manila has both urban and industrial local sources known to contribute to the dominance
960 of fine mode particles in its air (Cruz et al., 2019). Ten years of AERONET data in Manila
961 Observatory suggest that aerosol particles in Metro Manila were mixed in size but with a
962 prevalent fine mode fraction (>50% FMF) throughout the year. Background clean marine aerosol
963 particles (58% of the time) and fine polluted aerosol particles (20% of the time) were the most
964 dominant clear sky day sources impacting the atmospheric column over Metro Manila based on
965 cluster analysis of volume size distributions. The proximity of Metro Manila to the sea, both in
966 the east and west, along with local sources, transportation being the most prominent, together
967 contribute to the prevalence of the marine and fine particles. The prevalence of marine particles
968 could explain the relatively small AOD values in Metro Manila compared to other Southeast
969 Asian megacities (Reid et al., 2013).

970 Regional sources and meteorology also impact monthly aerosol optical depth trends in Metro
971 Manila from EOF analysis. Biomass burning from Borneo and Sumatra emerged in the study as
972 the second most prevalent regional anthropogenic aerosol particle source in Southeast Asia.
973 Though the monsoon trough limits the dispersion of aerosol particles throughout the entire
974 Southeast Asia, biomass burning emissions impact southern Southeast Asia including Metro
975 Manila during the southwest monsoon (July to September). The monsoon winds facilitate the
976 transport of fine particles during the peak burning season in Borneo and Sumatra (August-
977 September). This is experienced in Metro Manila as higher than usual aerosol particle loadings
978 around the same period (August to October). Climatologically, August was also when there were
979 particles with the greatest fine mode fractions that were relatively absorbing and non-
980 hygroscopic, possibly due to increased organic and elemental carbon fractional contributions.
981 Though not as strong a source as the Borneo and Sumatra case, the peninsular Southeast Asia
982 burning season (March-April) also contributed to extreme aerosol particle concentrations over
983 Metro Manila.

984 High aerosol particle loadings due to transported dust, probably from East Asia, were observed
985 in Metro Manila during the transition period between the southwest and northeast monsoons and
986 during the northeast monsoon (December to February). These extreme events are transient
987 because the lowest median aerosol particle loadings of the year were observed during the
988 northeast monsoon when annual wind speeds were highest. Particles then were observed to be
989 largest in diameter, with the greatest coarse fraction contribution, relatively high absorptivity,

990   and most hygrosocopicity, compared to other months of the year. This is probably due to
991   constituents other than soot, especially aged dust (Kim and Park, 2012; Geng et al., 2014) and
992   sea salt which the northeast winds appear to be bringing in from the general direction of the
993   Luzon Island and the Philippine Sea (West Pacific Ocean).

994   Cloud processing is one of the cases that were linked to very high aerosol particle loading in
995   Metro Manila. This is associated with sulfate sources, which appear more localized in nature
996   because of a power plant nearby. This sulfate source seems to be distinct from the industrial
997   sulfate air mass from East Asia, which is the most dominant regional aerosol particle source in
998   Southeast Asia (Li et al., 2013). Winds appear to limit the mixing of this notable East Asia air
999   mass with local industrial sources in the region including the Philippines and Indonesia.

1000   The formation of cloud systems in Southeast Asia is complex due to intersecting large- and
1001   small-scale mechanisms. Additionally, the interaction of particles and clouds in Southeast Asia is
1002   not yet well understood. In Metro Manila, both topography and meteorology affect aerosol
1003   particle distribution (Cruz et al., 2023). This baseline study on the aerosol particle characteristics
1004   in Metro Manila and in regional Southeast Asia shows how meteorology impacts varied aerosol
1005   particle sources (e.g., sulfate, elemental carbon, and organic carbon) and their distribution in the
1006   region. This can help in mitigating aerosol particle sources in the region and in the deepening of
1007   the understanding of the relationship of aerosol particles, meteorology, and clouds.
1008

1009   **Data availability**
1010   Aerosol Robotic Network (AERONET) (2020), Version 3 Direct Sun Algorithm, Site: Manila
1011   Observatory, Philippines, Accessed: [*28 September 2020*], https://aeronet.gsfc.nasa.gov/cgi-
1012   bin/webtool_aod_v3?stage=3&region=Asia&state=Philippines&site=Manila_Observatory&plac
1013   e_code=10&if_polarized=0

1014   Aerosol Robotic Network (AERONET) (2020), Version 3 Direct Sun and Inversion Algorithm,
1015   Site: Manila Observatory, Philippines, Accessed: [*28 September 2020*],
1016   https://aeronet.gsfc.nasa.gov/cgi-
1017   bin/webtool_inv_v3?stage=3&region=Asia&state=Philippines&site=Manila_Observatory&place
1018   _code=10&if_polarized=0

1019   Multi-angle Imaging SpectroRadiometer (MISR) Jet Propulsion Laboratory (2018), Level 3
1020   Component Global Aerosol product in netCDF format covering a month V004, Accessed: [*22
1021   November 2021],* https://search.earthdata.nasa.gov/

1022   Global Modeling and Assimilation Office (GMAO) (2015), MERRA-2 inst3_3d_asm_Np: 3d,3-
1023   Hourly, Instantaneous, Pressure-Level, Assimilation, Assimilated Meteorological Fields V5.12.4,
1024   Greenbelt, MD, USA, Goddard Earth Sciences Data and Information Services Center (GES
1025   DISC), Accessed: [*10 March 2021*], https://doi.org/10.5067/QBZ6MG944HW0

1026   Global Modeling and Assimilation Office (GMAO) (2015), MERRA-2 tavg1_2d_flx_Nx: 2d,1-
1027   Hourly, Time-Averaged, Single-Level, Assimilation, Surface Flux Diagnostics V5.12.4,
1028   Greenbelt, MD, USA, Goddard Earth Sciences Data and Information Services Center (GES
1029   DISC), Accessed: [*10 March 2021*], https://doi.org/10.5067/7MCPBJ41Y0K6

1030 Global Modeling and Assimilation Office (GMAO) (2015), MERRA-2 tavg1_2d_csp_Nx: 2d,1-
1031 Hourly, Time-averaged, Single-Level, Assimilation, COSP Satellite Simulator V5.12.4,
1032 Greenbelt, MD, USA, Goddard Earth Sciences Data and Information Services Center (GES
1033 DISC), Accessed: **[*13 July 2021*]**, https://doi.org/10.5067/H0VVAD8F6MX5

1034 Nguyen, P., E.J. Shearer, H. Tran, M. Ombadi, N. Hayatbini, T. Palacios, P. Huynh, G.
1035 Updegraff, K. Hsu, B. Kuligowski, W.S. Logan, and S. Sorooshian, The CHRS Data Portal, an
1036 easily accessible public repository for PERSIANN global satellite precipitation data, Nature
1037 Scientific Data, Vol. 6, Article 180296, 2019, Accessed: **[*11 March 2021*],**
1038 https://doi.org/10.1038/sdata.2018.296

1039
1040 Author contributions
1041 GRL and AS designed the experiment. NL, SNU, GRL, GFG, HJO, JBS, and MTC, carried out
1042 various aspects of the data collection. GRL, AS, JBS, MOC, MRH, CC, and LDG conducted
1043 analysis and interpretation of the data. GRL prepared the manuscript draft with contributions
1044 from the coauthors. AFA, LDG, MRH, GRL, and AS reviewed and edited the manuscript. AS
1045 led the management and funding acquisition. All authors approved the final version of the
1046 manuscript.
1047
1048 Competing interests
1049 We declare that Armin Sorooshian is a member of the editorial board of Atmospheric Chemistry
1050 and Physics. The peer-review process was guided by an independent editor, and the authors have
1051 also no other competing interests to declare.
1052
1053 Acknowledgements

1059

1060 References:

1061 AERONET Inversion Products (Version 3):
1062 https://aeronet.gsfc.nasa.gov/new_web/Documents/Inversion_products_for_V3.pdf, access: June
1063 25, 2021, 2019.

1064 Alas, H. D., Müller, T., Birmili, W., Kecorius, S., Cambaliza, M. O., Simpas, J. B. B., Cayetano,
1065 M., Weinhold, K., Vallar, E., and Galvez, M. C.: Spatial characterization of black carbon mass
1066 concentration in the atmosphere of a southeast asian megacity: an air quality case study for
1067 Metro Manila, Philippines, Aerosol Air Qual. Res., 18, 2301-2317,
1068 https://doi.org/10.4209/aaqr.2017.08.0281, 2018.

1069　Aldhaif, A. M., Lopez, D. H., Dadashazar, H., and Sorooshian, A.: Sources, frequency, and
1070　chemical nature of dust events impacting the United States East Coast, Atmos. Environ., 231,
1071　117456, https://doi.org/10.1016/j.atmosenv.2020.117456, 2020.

1072　Aldhaif, A. M., Lopez, D. H., Dadashazar, H., Painemal, D., Peters, A. J., and Sorooshian, A.:
1073　An Aerosol Climatology and Implications for Clouds at a Remote Marine Site: Case Study Over
1074　Bermuda, J. Geophys. Res.- Atmos., 126, e2020JD034038,
1075　https://doi.org/10.1029/2020JD034038, 2021.

1076　Alizadeh-Choobari, O., and Gharaylou, M.: Aerosol impacts on radiative and microphysical
1077　properties of clouds and precipitation formation, Atmos. Res., 185, 53-64,
1078　https://doi.org/10.1016/j.atmosres.2016.10.021, 2017.

1079　Amnuaylojaroen, T.: Air Pollution Modeling in Southeast Asia—An Overview, Vegetation Fires
1080　and Pollution in Asia, 531-544, https://doi.org/10.1007/978-3-031-29916-2_31, 2023.

1081　Ångström, A.: On the atmospheric transmission of sun radiation and on dust in the air,
1082　Geografiska Annaler, 11, 156-166, 1929.

1083　Arthur, D., and Vassilvitskii, S.: k-means++: The advantages of careful seeding, Stanford, 2006.

1084　AzadiAghdam, M., Braun, R. A., Edwards, E.-L., Bañaga, P. A., Cruz, M. T., Betito, G.,
1085　Cambaliza, M. O., Dadashazar, H., Lorenzo, G. R., and Ma, L.: On the nature of sea salt aerosol
1086　at a coastal megacity: Insights from Manila, Philippines in Southeast Asia, Atmos. Environ., 216,
1087　116922, https://doi.org/10.1016/j.atmosenv.2019.116922, 2019.

1088　Bagtasa, G.: Contribution of tropical cyclones to rainfall in the Philippines, Journal of Climate,
1089　30, 3621-3633, https://doi.org/10.1175/JCLI-D-16-0150.1, 2017.

1090　Bañares, E. N., Narisma, G. T. T., Simpas, J. B. B., Cruz, F. A. T., Lorenzo, G. R. H.,
1091　Cambaliza, M. O. L., and Coronel, R. C.: Seasonal and diurnal variations of observed convective
1092　rain events in metro Manila, Philippines, Atmos. Res., 105646,
1093　https://doi.org/10.1016/j.atmosres.2021.105646, 2021.

1094　Barth, M., Rasch, P., Kiehl, J., Benkovitz, C., and Schwartz, S.: Sulfur chemistry in the National
1095　Center for Atmospheric Research Community Climate Model: Description, evaluation, features,
1096　and sensitivity to aqueous chemistry, J. Geophys. Res.- Atmos., 105, 1387-1415,
1097　https://doi.org/10.1029/1999JD900773, 2000.

1098　Bautista VII, A. T., Pabroa, P. C. B., Santos, F. L., Racho, J. M. D., and Quirit, L. L.:
1099　Carbonaceous particulate matter characterization in an urban and a rural site in the Philippines,
1100　Atmospheric Pollution Research, 5, 245-252, https://doi.org/10.5094/APR.2014.030, 2014.

1101　Bergstrom, R. W., Russell, P. B., and Hignett, P.: Wavelength dependence of the absorption of
1102　black carbon particles: Predictions and results from the TARFOX experiment and implications
1103　for the aerosol single scattering albedo, J. Atmos. Sci., 59, 567-577,
1104　https://doi.org/10.1175/1520-0469(2002)059<0567:WDOTAO>2.0.CO;2, 2002.

Bergstrom, R. W., Pilewskie, P., Schmid, B., and Russell, P. B.: Estimates of the spectral aerosol single scattering albedo and aerosol radiative effects during SAFARI 2000, J. Geophys. Res.-Atmos., 108, https://doi.org/10.1029/2002JD002435, 2003.

Bergstrom, R. W., Pilewskie, P., Russell, P. B., Redemann, J., Bond, T. C., Quinn, P. K., and Sierau, B.: Spectral absorption properties of atmospheric aerosols, Atmos. Chem. Phys., 7, 5937-5943, https://doi.org/10.5194/acp-7-5937-2007, 2007.

Bi, J., Huang, J., Hu, Z., Holben, B., and Guo, Z.: Investigating the aerosol optical and radiative characteristics of heavy haze episodes in Beijing during January of 2013, J. Geophys. Res.-Atmos., 119, 9884-9900, https://doi.org/10.1002/2014JD021757, 2014.

Björnsson, H., and Venegas, S.: A manual for EOF and SVD analyses of climatic data, CCGCR Report, 97, 112-134, 1997.

Bohren, C. F., and Clothiaux, E. E.: Fundamentals of atmospheric radiation: an introduction with 400 problems, John Wiley & Sons, 2006.

Braun, R. A., Aghdam, M. A., Bañaga, P. A., Betito, G., Cambaliza, M. O., Cruz, M. T., Lorenzo, G. R., MacDonald, A. B., Simpas, J. B., and Stahl, C.: Long-range aerosol transport and impacts on size-resolved aerosol composition in Metro Manila, Philippines, Atmos. Chem. Phys., 20, 2387-2405, https://doi.org/10.5194/acp-20-2387-2020, 2020.

Buchard, V., Randles, C., Da Silva, A., Darmenov, A., Colarco, P., Govindaraju, R., Ferrare, R., Hair, J., Beyersdorf, A., and Ziemba, L.: The MERRA-2 aerosol reanalysis, 1980 onward. Part II: Evaluation and case studies, Journal of Climate, 30, 6851-6872, https://doi.org/10.1175/JCLI-D-16-0613.1, 2017.

Cahyono, W. E., Setyawati, W., Hamdi, S., Cholianawati, N., Kombara, P. Y., and Sari, W. J.: Observations of aerosol optical properties during tropical forest fires in Indonesia, Materials Today: Proceedings, 63, S445-S450, https://doi.org/10.1016/j.matpr.2022.04.113, 2022.

Caido, N. G., Ong, P. M., Rempillo, O., Galvez, M. C., and Vallar, E.: Spatiotemporal analysis of MODIS aerosol optical depth data in the Philippines from 2010 to 2020, Atmosphere, 13, 939, https://doi.org/10.3390/atmos13060939, 2022.

Chang, C.-P., Wang, Z., McBride, J., and Liu, C.-H.: Annual cycle of Southeast Asia—Maritime Continent rainfall and the asymmetric monsoon transition, Journal of climate, 18, 287-301, https://doi.org/10.1175/JCLI-3257.1, 2005.

Che, H., Xia, X., Zhu, J., Wang, H., Wang, Y., Sun, J., Zhang, X., and Shi, G.: Aerosol optical properties under the condition of heavy haze over an urban site of Beijing, China, Environ. Sci. Pollut. R., 22, 1043-1053, https://doi.org/10.1007/s11356-014-3415-5, 2015.

Chen, Q., McGowan, S., Gouramanis, C., Fong, L., Balasubramanian, R., and Taylor, D.: Rapidly rising transboundary atmospheric pollution from industrial and urban sources in Southeast Asia and its implications for regional sustainable development, Environ. Res. Lett., 15, 1040a1045, https://doi.org/10.1088/1748-9326/abb5ce, 2020.

Choi, M., Lim, H., Kim, J., Lee, S., Eck, T. F., Holben, B. N., Garay, M. J., Hyer, E. J., Saide, P. E., and Liu, H.: Validation, comparison, and integration of GOCI, AHI, MODIS, MISR, and VIIRS aerosol optical depth over East Asia during the 2016 KORUS-AQ campaign, Atmos. Meas. Tech., 12, 4619-4641, https://doi.org/10.5194/amt-12-4619-2019, 2019.

Cohen, J. B.: Quantifying the occurrence and magnitude of the Southeast Asian fire climatology, Environmental Research Letters, 9, 114018, https://dx.doi.org/10.1088/1748-9326/9/11/114018, 2014.

Cohen, J. B., Lecoeur, E., and Hui Loong Ng, D.: Decadal-scale relationship between measurements of aerosols, land-use change, and fire over Southeast Asia, Atmos. Chem. Phys., 17, 721-743, https://doi.org/10.5194/acp-17-721-2017, 2017.

Coronas, J.: The Climate and Weather of the Philippines, 1903-1918, by Rev. José Coronas. SJ, Chief, Meteorological Division, Weather Bureau, Manila Observatory, Manila,: Bureau of Printing, 1920.

Crosbie, E., Sorooshian, A., Monfared, N. A., Shingler, T., and Esmaili, O.: A multi-year aerosol characterization for the greater Tehran area using satellite, surface, and modeling data, Atmosphere, 5, 178-197, https://doi.org/10.3390/atmos5020178, 2014.

Crosbie, E., Ziemba, L. D., Shook, M. A., Robinson, C. E., Winstead, E. L., Thornhill, K. L., Braun, R. A., MacDonald, A. B., Stahl, C., and Sorooshian, A.: Measurement report: Closure analysis of aerosol–cloud composition in tropical maritime warm convection, Atmos. Chem. Phys., 22, 13269-13302, https://doi.org/10.5194/acp-22-13269-2022, 2022.

Cruz, F., Narisma, G. T., Villafuerte II, M. Q., Chua, K. C., and Olaguera, L. M.: A climatological analysis of the southwest monsoon rainfall in the Philippines, Atmos. Res., 122, 609-616, https://doi.org/10.1016/j.atmosres.2012.06.010, 2013.

Cruz, M. T., Bañaga, P. A., Betito, G., Braun, R. A., Stahl, C., Aghdam, M. A., Cambaliza, M. O., Dadashazar, H., Hilario, M. R., Lorenzo, G. R., Ma, L., MacDonald, A. B., Pabroa, C., Yee, J. R., Simpas, J. B., and Sorooshian, A.: Size-resolved composition and morphology of particulate matter during the southwest monsoon in Metro Manila, Philippines, Atmos. Chem. Phys., 19, 10675–10696, https://doi.org/10.5194/acp-19-10675-2019, 2019.

Cruz, M. T., Simpas, J. B., Sorooshian, A., Betito, G., Cambaliza, M. O. L., Collado, J. T., Eloranta, E. W., Holz, R., Topacio, X. G. V., and Del Socorro, J.: Impacts of regional wind circulations on aerosol pollution and planetary boundary layer structure in Metro Manila, Philippines, Atmos. Environ., 293, 119455, https://doi.org/10.1016/j.atmosenv.2022.119455, 2023.

Deep, A., Pandey, C. P., Nandan, H., Singh, N., Yadav, G., Joshi, P., Purohit, K., and Bhatt, S.: Aerosols optical depth and Ångström exponent over different regions in Garhwal Himalaya, India, Environmental Monitoring and Assessment, 193, 324, https://doi.org/10.1007/s10661-021-09048-4, 2021.

1179   Di Girolamo, L., Holz, R., Reid, J., Tanelli, S., van den Heever, S., Narsma, G., and Simpas, J.:
1180   Cloud and aerosol monsoonal processes-Philippines experiment (CAMP2Ex), NASA White
1181   Paper, 2015.

1182   Diner, D. J., Di Girolamo, L., and Nolin, A.: Preface to the MISR special issue, Remote Sens.
1183   Environ., 107, 1, https://doi.org/10.1016/j.rse.2006.11.001, 2007.

1184   Dong, X., and Fu, J. S.: Understanding interannual variations of biomass burning from
1185   Peninsular Southeast Asia, part II: Variability and different influences in lower and higher
1186   atmosphere levels, Atmospheric Environment, 115, 9-18,
1187   https://doi.org/10.1016/j.atmosenv.2015.05.052, 2015.

1188   Dorado, S. V., Holdsworth, J. L., Lagrosas, N. C., Villarin, J. R., Narisma, G., Ellis, J., and
1189   Perez, R.: Characterization of urban atmosphere of Manila with lidar, filter sampling, and
1190   radiosonde, Lidar Remote Sensing for Industry and Environment Monitoring, 2001, 591-598,

1191   Dubovik, O., Holben, B., Kaufman, Y., Yamasoe, M., Smirnov, A., Tanré, D., and Slutsker, I.:
1192   Single-scattering albedo of smoke retrieved from the sky radiance and solar transmittance
1193   measured from ground, J. Geophys. Res.- Atmos., 103, 31903-31923,
1194   https://doi.org/10.1029/98JD02276, 1998.

1195   Dubovik, O., and King, M. D.: A flexible inversion algorithm for retrieval of aerosol optical
1196   properties from Sun and sky radiance measurements, J. Geophys. Res.- Atmos., 105, 20673-
1197   20696, https://doi.org/10.1029/2000JD900282, 2000.

1198   Dubovik, O., Holben, B., Eck, T. F., Smirnov, A., Kaufman, Y. J., King, M. D., Tanré, D., and
1199   Slutsker, I.: Variability of absorption and optical properties of key aerosol types observed in
1200   worldwide locations, J. Atmos. Sci., 59, 590-608, https://doi.org/10.1175/1520-
1201   0469(2002)059<0590:VOAAOP>2.0.CO;2, 2002.

1202   Eck, T., Holben, B., Reid, J., O'neill, N., Schafer, J., Dubovik, O., Smirnov, A., Yamasoe, M.,
1203   and Artaxo, P.: High aerosol optical depth biomass burning events: A comparison of optical
1204   properties for different source regions, Geophys. Res. Lett., 30,
1205   https://doi.org/10.1029/2003GL017861, 2003.

1206   Eck, T., Holben, B., Dubovik, O., Smirnov, A., Goloub, P., Chen, H., Chatenet, B., Gomes, L.,
1207   Zhang, X. Y., and Tsay, S. C.: Columnar aerosol optical properties at AERONET sites in central
1208   eastern Asia and aerosol transport to the tropical mid-Pacific, J. Geophys. Res.- Atmos., 110,
1209   https://doi.org/10.1029/2004JD005274, 2005.

1210   Eck, T., Holben, B., Reid, J., Mukelabai, M., Piketh, S., Torres, O., Jethva, H., Hyer, E., Ward,
1211   D., and Dubovik, O.: A seasonal trend of single scattering albedo in southern African biomass-
1212   burning particles: Implications for satellite products and estimates of emissions for the world's
1213   largest biomass-burning source, J. Geophys. Res.- Atmos., 118, 6414-6432,
1214   https://doi.org/10.1002/jgrd.50500, 2013.

1215 Eck, T. F., Holben, B., Reid, J., Dubovik, O., Smirnov, A., O'neill, N., Slutsker, I., and Kinne, S.:
1216 Wavelength dependence of the optical depth of biomass burning, urban, and desert dust aerosols,
1217 J. Geophys. Res.- Atmos., 104, 31333-31349, https://doi.org/10.1029/1999JD900923, 1999.

1218 Eck, T. F., Holben, B. N., Reid, J., Giles, D., Rivas, M., Singh, R. P., Tripathi, S., Bruegge, C.,
1219 Platnick, S., and Arnold, G.: Fog-and cloud-induced aerosol modification observed by the
1220 Aerosol Robotic Network (AERONET), J. Geophys. Res.- Atmos., 117,
1221 https://doi.org/10.1029/2011JD016839, 2012.

1222 Edwards, E.-L., Reid, J. S., Xian, P., Burton, S. P., Cook, A. L., Crosbie, E. C., Fenn, M. A.,
1223 Ferrare, R. A., Freeman, S. W., and Hair, J. W.: Assessment of NAAPS-RA performance in
1224 Maritime Southeast Asia during CAMP 2 Ex, Atmospheric Chemistry and Physics, 22, 12961-
1225 12983, https://doi.org/10.5194/acp-22-12961-2022, 2022.

1226 Ervens, B., Sorooshian, A., Aldhaif, A. M., Shingler, T., Crosbie, E., Ziemba, L., Campuzano-
1227 Jost, P., Jimenez, J. L., and Wisthaler, A.: Is there an aerosol signature of chemical cloud
1228 processing?, Atmos. Chem. Phys., 18, 16099-16119, https://doi.org/10.5194/acp-18-16099-2018,
1229 2018.

1230 Faloona, I.: Sulfur processing in the marine atmospheric boundary layer: A review and critical
1231 assessment of modeling uncertainties, Atmos. Environ., 43, 2841-2854,
1232 https://doi.org/10.1016/j.atmosenv.2009.02.043, 2009.

1233 Feingold, G.: Modeling of the first indirect effect: Analysis of measurement requirements,
1234 Geophys. Res. Lett., 30, https://doi.org/10.1029/2003GL017967, 2003.

1235 Flores, J.: Climate of the Philippines, Climates of the Northern and Eastern Asia, 159-213, 1969.

1236 Formenti, P., Andreae, M. O., and Lelieveld, J.: Measurements of aerosol optical depth above
1237 3570 m asl in the North Atlantic free troposphere: results from ACE-2, Tellus B, 52, 678-693,
1238 https://doi.org/10.1034/j.1600-0889.2000.00006.x, 2000.

1239 Foth, A., Kanitz, T., Engelmann, R., Baars, H., Radenz, M., Seifert, P., Barja, B., Fromm, M.,
1240 Kalesse, H., and Ansmann, A.: Vertical aerosol distribution in the southern hemispheric
1241 midlatitudes as observed with lidar in Punta Arenas, Chile (53.2∘ S and 70.9∘ W), during
1242 ALPACA, Atmospheric Chemistry and Physics, 19, 6217-6233, https://doi.org/10.5194/acp-19-
1243 6217-2019, 2019.

1244 Garay, M. J., Bull, M. A., Nastan, A. M., Witek, M. L., Seidel, F. C., Diner, D. J., Kahn, R. A.,
1245 Limbacher, J. A., and Kalashnikova, O. V.: Data Product Specification for the MISR Level 2
1246 Aerosol Product, Jet Propulsion Laboratory, California Institute of Technology. JPL D-100649.
1247 https://asdc.larc.nasa.gov/documents/misr/DPS_AEROSOL_V023.20180125.pdf, 2018.

1248 Gautam, R., Hsu, N. C., Eck, T. F., Holben, B. N., Janjai, S., Jantarach, T., Tsay, S.-C., and Lau,
1249 W. K.: Characterization of aerosols over the Indochina peninsula from satellite-surface
1250 observations during biomass burning pre-monsoon season, Atmos. Environ., 78, 51-59,
1251 https://doi.org/10.1016/j.atmosenv.2012.05.038, 2013.

1252 Gelaro, R., McCarty, W., Suárez, M. J., Todling, R., Molod, A., Takacs, L., Randles, C. A.,
1253 Darmenov, A., Bosilovich, M. G., and Reichle, R.: The modern-era retrospective analysis for
1254 research and applications, version 2 (MERRA-2), J. Climate, 30, 5419-5454,
1255 https://doi.org/10.1175/JCLI-D-16-0758.1, 2017.

1256 Geng, H., Hwang, H., Liu, X., Dong, S., and Ro, C.-U.: Investigation of aged aerosols in size-
1257 resolved Asian dust storm particles transported from Beijing, China, to Incheon, Korea, using
1258 low-Z particle EPMA, Atmos. Chem. Phys., 14, 3307-3323, https://doi.org/10.5194/acp-14-
1259 3307-2014, 2014.

1260 Giles, D. M., Holben, B. N., Eck, T. F., Sinyuk, A., Smirnov, A., Slutsker, I., Dickerson, R.,
1261 Thompson, A., and Schafer, J.: An analysis of AERONET aerosol absorption properties and
1262 classifications representative of aerosol source regions, J. Geophys. Res.- Atmos., 117,
1263 https://doi.org/10.1029/2012JD018127, 2012.

1264 Giles, D. M., Sinyuk, A., Sorokin, M. G., Schafer, J. S., Smirnov, A., Slutsker, I., Eck, T. F.,
1265 Holben, B. N., Lewis, J. R., and Campbell, J. R.: Advancements in the Aerosol Robotic Network
1266 (AERONET) Version 3 database–automated near-real-time quality control algorithm with
1267 improved cloud screening for Sun photometer aerosol optical depth (AOD) measurements,
1268 Atmos. Meas. Tech., 12, 169-209, https://doi.org/10.5194/amt-12-169-2019, 2019.

1269 Glover, D., and Jessup, T.: The Indonesian fires and haze of 1997: the economic toll, Economy
1270 and Environment Program for SE Asia (EEPSEA) Singapore and the World Wildlife Fund
1271 (WWF) Indonesia, Jakarta, 1998.

1272 Guyon, P., Boucher, O., Graham, B., Beck, J., Mayol-Bracero, O. L., Roberts, G. C., Maenhaut,
1273 W., Artaxo, P., and Andreae, M. O.: Refractive index of aerosol particles over the Amazon
1274 tropical forest during LBA-EUSTACH 1999, J. Aerosol Sci., 34, 883-907,
1275 https://doi.org/10.1016/S0021-8502(03)00052-1, 2003.

1276 Harenda, K. M., Markowicz, K. M., Poczta, P., Stachlewska, I. S., Bojanowski, J. S., Czernecki,
1277 B., McArthur, A., Schuetemeyer, D., and Chojnicki, B. H.: Estimation of the effects of aerosol
1278 optical properties on peatland production in Rzecin, Poland, Agricultural and Forest
1279 Meteorology, 316, 108861, https://doi.org/10.1016/j.agrformet.2022.108861, 2022.

1280 Hartley, W. S., and Hobbs, P. V.: An aerosol model and aerosol-induced changes in the clear-sky
1281 albedo off the east coast of the United States, J. Geophys. Res.- Atmos., 106, 9733-9748,
1282 https://doi.org/10.1029/2001JD900025, 2001.

1283 Haywood, J., and Boucher, O.: Estimates of the direct and indirect radiative forcing due to
1284 tropospheric aerosols: A review, Rev. Geophys., 38, 513-543,
1285 https://doi.org/10.1029/1999RG000078, 2000.

1286 Hendrickson, B. N., Brooks, S. D., Thornton, D. C., Moore, R. H., Crosbie, E., Ziemba, L. D.,
1287 Carlson, C. A., Baetge, N., Mirrielees, J. A., and Alsante, A. N.: Role of sea surface microlayer
1288 properties in cloud formation, Frontiers in Marine Science, 7, 596225,
1289 https://doi.org/10.3389/fmars.2020.596225, 2021.

Herber, A., Thomason, L. W., Gernandt, H., Leiterer, U., Nagel, D., Schulz, K. H., Kaptur, J., Albrecht, T., and Notholt, J.: Continuous day and night aerosol optical depth observations in the Arctic between 1991 and 1999, J. Geophys. Res.- Atmos., 107, AAC 6-1-AAC 6-13, https://doi.org/10.1029/2001JD000536, 2002.

Hilario, M. R. A., Cruz, M. T., Bañaga, P. A., Betito, G., Braun, R. A., Stahl, C., Cambaliza, M. O., Lorenzo, G. R., MacDonald, A. B., AzadiAghdam, M., Pabroa, P. C., Yee, J. R., Simpas, J. B., and Sorooshian, A.: Characterizing weekly cycles of particulate matter in a coastal megacity: The importance of a seasonal, size-resolved, and chemically-speciated analysis, J. Geophys. Res.- Atmos., 125, e2020JD032614, https://doi.org/10.1029/2020JD032614, 2020a.

Hilario, M. R. A., Cruz, M. T., Cambaliza, M. O. L., Reid, J. S., Xian, P., Simpas, J. B., Lagrosas, N. D., Uy, S. N. Y., Cliff, S., and Zhao, Y.: Investigating size-segregated sources of elemental composition of particulate matter in the South China Sea during the 2011 Vasco cruise, Atmos. Chem. Phys., 20, 1255-1276, https://doi.org/10.5194/acp-20-1255-2020, 2020b.

Hilario, M. R. A., Crosbie, E., Shook, M., Reid, J. S., Cambaliza, M. O. L., Simpas, J. B. B., Ziemba, L., DiGangi, J. P., Diskin, G. S., and Nguyen, P.: Measurement report: Long-range transport patterns into the tropical northwest Pacific during the CAMP 2 Ex aircraft campaign: chemical composition, size distributions, and the impact of convection, Atmos. Chem. Phys., 21, 3777-3802, https://doi.org/10.5194/acp-21-3777-2021, 2021a.

Hilario, M. R. A., Olaguera, L. M., Narisma, G. T., and Matsumoto, J.: Diurnal characteristics of summer precipitation over Luzon Island, Philippines, Asia-Pacific Journal of Atmospheric Sciences, 57, 573-585, https://doi.org/10.1007/s13143-020-00214-1, 2021b.

Hilario, M. R. A., Bañaga, P. A., Betito, G., Braun, R. A., Cambaliza, M. O., Cruz, M. T., Lorenzo, G. R., MacDonald, A. B., Pabroa, P. C., and Simpas, J. B.: Stubborn aerosol: why particulate mass concentrations do not drop during the wet season in Metro Manila, Philippines, Environmental Science: Atmospheres, 2, 1428-1437, https://doi.org/10.1039/D2EA00073C, 2022.

Hogan, T. F., Liu, M., Ridout, J. A., Peng, M. S., Whitcomb, T. R., Ruston, B. C., Reynolds, C. A., Eckermann, S. D., Moskaitis, J. R., and Baker, N. L.: The navy global environmental model, Oceanography, 27, 116-125, https://doi.org/10.5670/oceanog.2014.73, 2014.

Holben, B. N., Eck, T. F., Slutsker, I. a., Tanre, D., Buis, J., Setzer, A., Vermote, E., Reagan, J. A., Kaufman, Y., and Nakajima, T.: AERONET—A federated instrument network and data archive for aerosol characterization, Remote Sens. Environ., 66, 1-16, https://doi.org/10.1016/S0034-4257(98)00031-5, 1998.

Holben, B. N., Tanre, D., Smirnov, A., Eck, T., Slutsker, I., Abuhassan, N., Newcomb, W., Schafer, J., Chatenet, B., and Lavenu, F.: An emerging ground-based aerosol climatology: Aerosol optical depth from AERONET, J. Geophys. Res.- Atmos., 106, 12067-12097, https://doi.org/10.1029/2001JD900014, 2001.

Hong, Y., and Di Girolamo, L.: Cloud phase characteristics over Southeast Asia from A-Train satellite observations, Atmos. Chem. Phys., 20, 8267-8291, https://doi.org/10.5194/acp-20-8267-2020, 2020.

Hong, Y., and Di Girolamo, L.: An overview of aerosol properties in clear and cloudy sky based on CALIPSO observations, Earth and Space Science, 9, e2022EA002287, https://doi.org/10.1029/2022EA002287, 2022.

Hoppel, W., Frick, G., Fitzgerald, J., and Larson, R.: Marine boundary layer measurements of new particle formation and the effects nonprecipitating clouds have on aerosol size distribution, J. Geophys. Res.- Atmos., 99, 14443-14459, https://doi.org/10.1029/94JD00797, 1994.

Huang, C., Li, J., Sun, W., Chen, Q., Mao, Q.-J., and Yuan, Y.: Long-Term Variation Assessment of Aerosol Load and Dominant Types over Asia for Air Quality Studies Using Multi-Sources Aerosol Datasets, Remote Sensing, 13, 3116, https://doi.org/10.3390/rs13163116, 2021.

Hyer, E. J., Reid, J. S., Prins, E. M., Hoffman, J. P., Schmidt, C. C., Miettinen, J. I., and Giglio, L.: Patterns of fire activity over Indonesia and Malaysia from polar and geostationary satellite observations, Atmos. Res., 122, 504-519, https://doi.org/10.1016/j.atmosres.2012.06.011, 2013.

Jamora, J. B., Gudia, S. E. L., Go, A. W., Giduquio, M. B., and Loretero, M. E.: Potential CO2 reduction and cost evaluation in use and transport of coal ash as cement replacement: A case in the Philippines, Waste Manage., 103, 137-145, https://doi.org/10.1016/j.wasman.2019.12.026, 2020.

Jose, S., Gharai, B., Niranjan, K., and Rao, P.: Investigation on seasonal variations of aerosol properties and its influence on radiative effect over an urban location in central India, Atmos. Environ., 133, 41-48, https://doi.org/10.1016/j.atmosenv.2016.03.029, 2016.

Kaskaoutis, D., Kosmopoulos, P., Kambezidis, H., and Nastos, P.: Aerosol climatology and discrimination of different types over Athens, Greece, based on MODIS data, Atmos. Environ., 41, 7315-7329, https://doi.org/10.1016/j.atmosenv.2007.05.017, 2007.

Kaskaoutis, D., Badarinath, K., Kumar Kharol, S., Rani Sharma, A., and Kambezidis, H.: Variations in the aerosol optical properties and types over the tropical urban site of Hyderabad, India, Journal of Geophysical Research: Atmospheres, 114, https://doi.org/10.1029/2009JD012423, 2009.

Kiely, L., Spracklen, D. V., Wiedinmyer, C., Conibear, L., Reddington, C. L., Archer-Nicholls, S., Lowe, D., Arnold, S. R., Knote, C., and Khan, M. F.: New estimate of particulate emissions from Indonesian peat fires in 2015, Atmospheric Chemistry and Physics, 19, 11105-11121, https://doi.org/10.5194/acp-19-11105-2019, 2019.

Kim, J.-S., and Park, K.: Atmospheric aging of Asian dust particles during long range transport, Aerosol Sci. Tech., 46, 913-924, https://doi.org/10.1080/02786826.2012.680984, 2012.

Kirchstetter, T. W., Novakov, T., and Hobbs, P. V.: Evidence that the spectral dependence of light absorption by aerosols is affected by organic carbon, J. Geophys. Res.- Atmos., 109, https://doi.org/10.1029/2004JD004999, 2004.

Koven, C. D., and Fung, I.: Inferring dust composition from wavelength-dependent absorption in Aerosol Robotic Network (AERONET) data, J. Geophys. Res.- Atmos., 111, https://doi.org/10.1029/2005JD006678, 2006.

Kudo, R., Nishizawa, T., and Aoyagi, T.: Vertical profiles of aerosol optical properties and the solar heating rate estimated by combining sky radiometer and lidar measurements, Atmos. Meas. Tech., 9, 3223-3243, https://doi.org/10.5194/amt-9-3223-2016, 2016.

Kumar, K. R., Sivakumar, V., Reddy, R. R., Gopal, K. R., and Adesina, A. J.: Identification and classification of different aerosol types over a subtropical rural site in Mpumalanga, South Africa: seasonal variations as retrieved from the AERONET Sunphotometer, Aerosol Air Qual. Res., 14, 108-123, https://doi.org/10.4209/aaqr.2013.03.0079, 2014.

Kumar, K. R., Yin, Y., Sivakumar, V., Kang, N., Yu, X., Diao, Y., Adesina, A. J., and Reddy, R.: Aerosol climatology and discrimination of aerosol types retrieved from MODIS, MISR and OMI over Durban (29.88 S, 31.02 E), South Africa, Atmos. Environ., 117, 9-18, https://doi.org/10.1016/j.atmosenv.2015.06.058, 2015.

Kuttippurath, J., and Raj, S.: Two decades of aerosol observations by AATSR, MISR, MODIS and MERRA-2 over India and Indian Ocean, Remote Sens. Environ., 257, 112363, https://doi.org/10.1016/j.rse.2021.112363, 2021.

Lee, H.-H., Iraqui, O., Gu, Y., Yim, S. H.-L., Chulakadabba, A., Tonks, A. Y.-M., Yang, Z., and Wang, C.: Impacts of air pollutants from fire and non-fire emissions on the regional air quality in Southeast Asia, Atmos. Chem. Phys., 18, 6141-6156, https://doi.org/10.5194/acp-18-6141-2018, 2018.

Lee, J., Kim, J., Song, C., Kim, S., Chun, Y., Sohn, B., and Holben, B.: Characteristics of aerosol types from AERONET sunphotometer measurements, Atmospheric Environment, 44, 3110-3117, https://doi.org/10.1016/j.atmosenv.2010.05.035, 2010.

Li, G., Bei, N., Cao, J., Huang, R., Wu, J., Feng, T., Wang, Y., Liu, S., Zhang, Q., and Tie, X.: A possible pathway for rapid growth of sulfate during haze days in China, Atmos. Chem. Phys., 17, 3301-3316, https://doi.org/10.5194/acp-17-3301-2017, 2017.

Li, J., Carlson, B. E., and Lacis, A. A.: Application of spectral analysis techniques in the intercomparison of aerosol data: 1. An EOF approach to analyze the spatial-temporal variability of aerosol optical depth using multiple remote sensing data sets, J. Geophys. Res.- Atmos., 118, 8640-8648, https://doi.org/10.1002/jgrd.50686, 2013.

Li, Z., Niu, F., Fan, J., Liu, Y., Rosenfeld, D., and Ding, Y.: Long-term impacts of aerosols on the vertical development of clouds and precipitation, Nat. Geosci., 4, 888-894, https://doi.org/10.1038/ngeo1313, 2011.

Lin, N.-H., Sayer, A. M., Wang, S.-H., Loftus, A. M., Hsiao, T.-C., Sheu, G.-R., Hsu, N. C., Tsay, S.-C., and Chantara, S.: Interactions between biomass-burning aerosols and clouds over Southeast Asia: Current status, challenges, and perspectives, Environ. Pollut., 195, 292-307, https://doi.org/10.1016/j.envpol.2014.06.036, 2014.

Lloyd, S.: Least squares quantization in PCM, IEEE T. Inform. Theory, 28, 129-137, https://doi.org/10.1109/TIT.1982.1056489, 1982.

Lynch, P., Reid, J. S., Westphal, D. L., Zhang, J., Hogan, T. F., Hyer, E. J., Curtis, C. A., Hegg, D. A., Shi, Y., and Campbell, J. R.: An 11-year global gridded aerosol optical thickness reanalysis (v1. 0) for atmospheric and climate sciences, Geosci. Model Dev., 9, https://doi.org/10.5194/gmd-9-1489-2016, 2016.

Markowicz, K., Zawadzka-Manko, O., Lisok, J., Chilinski, M., and Xian, P.: The impact of moderately absorbing aerosol on surface sensible, latent, and net radiative fluxes during the summer of 2015 in Central Europe, Journal of Aerosol Science, 151, 105627, https://doi.org/10.1016/j.jaerosci.2020.105627, 2021.

Matsumoto, J., Olaguera, L. M. P., Nguyen-Le, D., Kubota, H., and Villafuerte, M. Q.: Climatological seasonal changes of wind and rainfall in the Philippines, Int. J. Climatol., 40, 4843-4857, https://doi.org/10.1002/joc.6492, 2020.

Mims III, F. M.: A 30-Year Climatology (1990–2020) of Aerosol Optical Depth and Total Column Water Vapor and Ozone over Texas, Bulletin of the American Meteorological Society, 103, E101-E109, https://doi.org/10.1175/BAMS-D-21-0010.1, 2022.

Moosmüller, H., and Sorensen, C.: Small and large particle limits of single scattering albedo for homogeneous, spherical particles, J. Quant. Spectrosc. Ra., 204, 250-255, https://doi.org/10.1016/j.jqsrt.2017.09.029, 2018.

Mora, M., Braun, R. A., Shingler, T., and Sorooshian, A.: Analysis of remotely sensed and surface data of aerosols and meteorology for the Mexico Megalopolis Area between 2003 and 2015, J. Geophys. Res.- Atmos., 122, 8705-8723, https://doi.org/10.1002/2017JD026739, 2017.

Nakata, M., Mukai, S., and Yasumoto, M.: Seasonal and regional characteristics of aerosol pollution in east and southeast Asia, Frontiers in Environmental Science, 6, 29, https://doi.org/10.3389/fenvs.2018.00029, 2018.

Fires and Smoke in Borneo: https://earthobservatory.nasa.gov/images/40182/fires-and-smoke-in-borneo), 2009.

Nguyen, P., Shearer, E. J., Tran, H., Ombadi, M., Hayatbini, N., Palacios, T., Huynh, P., Braithwaite, D., Updegraff, G., and Hsu, K.: The CHRS Data Portal, an easily accessible public repository for PERSIANN global satellite precipitation data, Scientific Data, 6, 1-10, https://doi.org/10.1038/sdata.2018.296, 2019a.

Nguyen, T. T., Pham, H. V., Lasko, K., Bui, M. T., Laffly, D., Jourdan, A., and Bui, H. Q.: Spatiotemporal analysis of ground and satellite-based aerosol for air quality assessment in the

1437 Southeast Asia region, Environmental Pollution, 255, 113106,
1438 https://doi.org/10.1016/j.envpol.2019.113106, 2019b.

1439 North, G. R., Bell, T. L., Cahalan, R. F., and Moeng, F. J.: Sampling errors in the estimation of
1440 empirical orthogonal functions, Mon. Weather Rev., 110, 699-706, https://doi.org/10.1175/1520-
1441 0493(1982)110<0699:SEITEO>2.0.CO;2, 1982.

1442 O'Neill, N., Eck, T., Smirnov, A., Holben, B., and Thulasiraman, S.: Spectral discrimination of
1443 coarse and fine mode optical depth, J. Geophys. Res.- Atmos., 108,
1444 https://doi.org/10.1029/2002JD002975, 2003.

1445 Oanh, N. K., Upadhyay, N., Zhuang, Y.-H., Hao, Z.-P., Murthy, D., Lestari, P., Villarin, J.,
1446 Chengchua, K., Co, H., and Dung, N.: Particulate air pollution in six Asian cities: Spatial and
1447 temporal distributions, and associated sources, Atmospheric environment, 40, 3367-3380,
1448 https://doi.org/10.1016/j.atmosenv.2006.01.050, 2006.

1449 Oanh, N. T. K., Permadi, D. A., Hopke, P. K., Smith, K. R., Dong, N. P., and Dang, A. N.:
1450 Annual emissions of air toxics emitted from crop residue open burning in Southeast Asia over
1451 the period of 2010–2015, Atmos. Environ., 187, 163-173,
1452 https://doi.org/10.1016/j.atmosenv.2018.05.061, 2018.

1453 Ong, H. J. J., Lagrosas, N., Uy, S. N., Gacal, G. F. B., Dorado, S., Tobias Jr, V., and Holben, B.:
1454 Determination of Monthly Aerosol Types in Manila Observatory and Notre Dame of Marbel
1455 University from Aerosol Robotic Network (AERONET) measurements, AGU Fall Meeting
1456 Abstracts, 2016, A54E-03,

1457 Pace, G., Sarra, A. d., Meloni, D., Piacentino, S., and Chamard, P.: Aerosol optical properties at
1458 Lampedusa (Central Mediterranean). 1. Influence of transport and identification of different
1459 aerosol types, Atmos. Chem. Phys., 6, 697-713, https://doi.org/10.5194/acp-6-697-2006, 2006.

1460 Pandolfi, M., Alados-Arboledas, L., Alastuey, A., Andrade, M., Angelov, C., Artiñano, B.,
1461 Backman, J., Baltensperger, U., Bonasoni, P., and Bukowiecki, N.: A European aerosol
1462 phenomenology–6: scattering properties of atmospheric aerosol particles from 28 ACTRIS sites,
1463 Atmos. Chem. Phys., 18, 7877-7911, https://doi.org/10.5194/acp-18-7877-2018, 2018.

1464 Petters, M. D., Carrico, C. M., Kreidenweis, S. M., Prenni, A. J., DeMott, P. J., Collett Jr, J. L.,
1465 and Moosmüller, H.: Cloud condensation nucleation activity of biomass burning aerosol, J.
1466 Geophys. Res.- Atmos., 114, https://doi.org/10.1029/2009JD012353, 2009.

1467 Plymale, N. T., Szekely, J. E., and Rubinstein, A. H.: Statistical Cluster Analysis of Global
1468 Aerosol Optical Depth for Simplified Atmospheric Modeling, J. Appl. Meteorol. Clim.,
1469 https://doi.org/10.1175/JAMC-D-21-0150.1, 2021.

1470 PSA: Highlights of the Philippine population 2015 census of population, Philippine Statistics
1471 Authority, 2016.

Qi, Y., Ge, J., and Huang, J.: Spatial and temporal distribution of MODIS and MISR aerosol optical depth over northern China and comparison with AERONET, Chinese science bulletin, 58, 2497-2506, https://doi.org/10.1007/s11434-013-5678-5, 2013.

Ramage, C. S.: Monsoon meteorology, Academic Press, New York, 1971.

Randles, C., Da Silva, A., Buchard, V., Colarco, P., Darmenov, A., Govindaraju, R., Smirnov, A., Holben, B., Ferrare, R., and Hair, J.: The MERRA-2 aerosol reanalysis, 1980 onward. Part I: System description and data assimilation evaluation, J. Climate, 30, 6823-6850, https://doi.org/10.1175/JCLI-D-16-0609.1, 2017.

Reid, J., Koppmann, R., Eck, T., and Eleuterio, D.: A review of biomass burning emissions part II: intensive physical properties of biomass burning particles, Atmos. Chem. Phys., 5, 799-825, https://doi.org/10.5194/acp-5-799-2005, 2005.

Reid, J., Xian, P., Hyer, E., Flatau, M., Ramirez, E., Turk, F., Sampson, C., Zhang, C., Fukada, E., and Maloney, E.: Multi-scale meteorological conceptual analysis of observed active fire hotspot activity and smoke optical depth in the Maritime Continent, Atmos. Chem. Phys., 12, 2117, https://doi.org/10.5194/acp-12-2117-2012, 2012.

Reid, J., Maring, H., Narisma, G., van den Heever, S., Di Girolamo, L., Ferrare, R., Holz, R., Lawson, P., Mace, G., and Simpas, J.: The coupling between tropical meteorology, aerosol lifecycle, convection, and radiation, during the Cloud, Aerosol and Monsoon Processes Philippines Experiment (CAMP 2 Ex), B. Am. Meteorol. Soc., https://doi.org/10.1175/BAMS-D-21-0285.1, 2023.

Reid, J. S., Hobbs, P. V., Liousse, C., Martins, J. V., Weiss, R. E., and Eck, T. F.: Comparisons of techniques for measuring shortwave absorption and black carbon content of aerosols from biomass burning in Brazil, J. Geophys. Res.- Atmos., 103, 32031-32040, https://doi.org/10.1029/98JD00773, 1998.

Reid, J. S., Hyer, E. J., Johnson, R. S., Holben, B. N., Yokelson, R. J., Zhang, J., Campbell, J. R., Christopher, S. A., Di Girolamo, L., and Giglio, L.: Observing and understanding the Southeast Asian aerosol system by remote sensing: An initial review and analysis for the Seven Southeast Asian Studies (7SEAS) program, Atmos. Res., 122, 403-468, https://doi.org/10.1016/j.atmosres.2012.06.005, 2013.

Reid, J. S., Lagrosas, N. D., Jonsson, H. H., Reid, E. A., Sessions, W. R., Simpas, J. B., Uy, S. N., Boyd, T., Atwood, S. A., and Blake, D. R.: Observations of the temporal variability in aerosol properties and their relationships to meteorology in the summer monsoonal South China Sea/East Sea: the scale-dependent role of monsoonal flows, the Madden–Julian Oscillation, tropical cyclones, squall lines and cold pools, Atmos. Chem. Phys., 15, 1745-1768, https://doi.org/10.5194/acp-15-1745-2015, 2015.

Rizza, U., Mancinelli, E., Morichetti, M., Passerini, G., and Virgili, S.: Aerosol optical depth of the main aerosol species over Italian cities based on the NASA/MERRA-2 model reanalysis, Atmosphere, 10, 709, https://doi.org/10.3390/atmos10110709, 2019.

Rolph, G., Stein, A., and Stunder, B.: Real-time environmental applications and display system: READY, Environ. Modell. Softw., 95, 210-228, https://doi.org/10.1016/j.envsoft.2017.06.025, 2017.

Ross, A. D., Holz, R. E., Quinn, G., Reid, J. S., Xian, P., Turk, F. J., and Posselt, D. J.: Exploring the first aerosol indirect effect over Southeast Asia using a 10-year collocated MODIS, CALIOP, and model dataset, Atmospheric Chemistry and Physics, 18, 12747-12764, https://doi.org/10.5194/acp-18-12747-2018, 2018.

Ross, J. L., Hobbs, P. V., and Holben, B.: Radiative characteristics of regional hazes dominated by smoke from biomass burning in Brazil: Closure tests and direct radiative forcing, J. Geophys. Res.- Atmos., 103, 31925-31941, https://doi.org/10.1029/97JD03677, 1998.

Saleh, R., Hennigan, C., McMeeking, G., Chuang, W., Robinson, E., Coe, H., Donahue, N., and Robinson, A.: Absorptivity of brown carbon in fresh and photo-chemically aged biomass-burning emissions, Atmos. Chem. Phys., 13, 7683-7693, https://doi.org/10.5194/acp-13-7683-2013, 2013.

Schlosser, J. S., Braun, R. A., Bradley, T., Dadashazar, H., MacDonald, A. B., Aldhaif, A. A., Aghdam, M. A., Mardi, A. H., Xian, P., and Sorooshian, A.: Analysis of aerosol composition data for western United States wildfires between 2005 and 2015: Dust emissions, chloride depletion, and most enhanced aerosol constituents, J. Geophys. Res.- Atmos., 122, 8951-8966, https://doi.org/10.1002/2017JD026547, 2017.

Schuster, G., Dubovik, O., and Arola, A.: Remote sensing of soot carbon–Part 1: Distinguishing different absorbing aerosol species, Atmos. Chem. Phys., 16, 1565-1585, https://doi.org/10.5194/acp-16-1565-2016, 2016.

Schuster, G. L., Dubovik, O., and Holben, B. N.: Angstrom exponent and bimodal aerosol size distributions, J. Geophys. Res.- Atmos., 111, https://doi.org/10.1029/2005JD006328, 2006.

Sharma, M., Kaskaoutis, D. G., Singh, R. P., and Singh, S.: Seasonal variability of atmospheric aerosol parameters over Greater Noida using ground sunphotometer observations, Aerosol Air Qual. Res., 14, 608-622, https://doi.org/10.4209/aaqr.2013.06.0219, 2014.

Shen, Z., Liu, J., Horowitz, L., Henze, D., Fan, S., Mauzerall, D. L., Lin, J.-T., and Tao, S.: Analysis of transpacific transport of black carbon during HIPPO-3: implications for black carbon aging, Atmos. Chem. Phys., 14, 6315-6327, https://doi.org/10.5194/acp-14-6315-2014, 2014.

Sinyuk, A., Holben, B. N., Eck, T. F., Giles, D. M., Slutsker, I., Korkin, S., Schafer, J. S., Smirnov, A., Sorokin, M., and Lyapustin, A.: The AERONET Version 3 aerosol retrieval algorithm, associated uncertainties and comparisons to Version 2, Atmospheric Measurement Techniques, 13, 3375-3411, https://doi.org/10.5194/amt-13-3375-2020, 2020.

Smirnov, A., Holben, B. N., Dubovik, O., O'Neill, N. T., Eck, T. F., Westphal, D. L., Goroch, A. K., Pietras, C., and Slutsker, I.: Atmospheric aerosol optical properties in the Persian Gulf, J. Atmos. Sci., 59, 620-634, https://doi.org/10.1175/1520-0469(2002)059<0620:AAOPIT>2.0.CO;2, 2002.

1548 Smith, S. J., Aardenne, J. v., Klimont, Z., Andres, R. J., Volke, A., and Delgado Arias, S.:
1549 Anthropogenic sulfur dioxide emissions: 1850–2005, Atmos. Chem. Phys., 11, 1101-1116,
1550 https://doi.org/10.5194/acp-11-1101-2011, 2011.

1551 Sorooshian, A., Wang, Z., Feingold, G., and L'Ecuyer, T. S.: A satellite perspective on cloud
1552 water to rain water conversion rates and relationships with environmental conditions, J.
1553 Geophys. Res.- Atmos., 118, 6643-6650, https://doi.org/10.1002/jgrd.50523, 2013.

1554 Stahl, C., Cruz, M. T., Bañaga, P. A., Betito, G., Braun, R. A., Aghdam, M. A., Cambaliza, M.
1555 O., Lorenzo, G. R., MacDonald, A. B., and Hilario, M. R. A.: Sources and characteristics of size-
1556 resolved particulate organic acids and methanesulfonate in a coastal megacity: Manila,
1557 Philippines, Atmos. Chem. Phys., 20, 15907-15935, https://doi.org/10.5194/acp-20-15907-2020,
1558 2020.

1559 Stahl, C., Crosbie, E., Bañaga, P. A., Betito, G., Braun, R. A., Cainglet, Z. M., Cambaliza, M. O.,
1560 Cruz, M. T., Dado, J. M., and Hilario, M. R. A.: Total organic carbon and the contribution from
1561 speciated organics in cloud water: airborne data analysis from the CAMP 2 Ex field campaign,
1562 Atmos. Chem. Phys., 21, 14109-14129, https://doi.org/10.5194/acp-21-14109-2021, 2021.

1563 Stein, A., Draxler, R. R., Rolph, G. D., Stunder, B. J., Cohen, M., and Ngan, F.: NOAA's
1564 HYSPLIT atmospheric transport and dispersion modeling system, B. Am. Meteorol. Soc., 96,
1565 2059-2077, https://doi.org/10.1175/BAMS-D-14-00110.1, 2015.

1566 Stevens, B., and Feingold, G.: Untangling aerosol effects on clouds and precipitation in a
1567 buffered system, Nature, 461, 607-613, https://doi.org/10.1038/nature08281, 2009.

1568 Sullivan, R. C., Levy, R. C., da Silva, A. M., and Pryor, S. C.: Developing and diagnosing
1569 climate change indicators of regional aerosol optical properties, Scientific Reports, 7, 1-13,
1570 https://doi.org/10.1038/s41598-017-18402-x, 2017.

1571 Tao, W. K., Chen, J. P., Li, Z., Wang, C., and Zhang, C.: Impact of aerosols on convective
1572 clouds and precipitation, Rev. Geophys., 50, https://doi.org/10.1029/2011RG000369, 2012.

1573 Tsay, S.-C., Hsu, N. C., Lau, W. K.-M., Li, C., Gabriel, P. M., Ji, Q., Holben, B. N., Welton, E.
1574 J., Nguyen, A. X., and Janjai, S.: From BASE-ASIA toward 7-SEAS: A satellite-surface
1575 perspective of boreal spring biomass-burning aerosols and clouds in Southeast Asia,
1576 Atmospheric environment, 78, 20-34, https://doi.org/10.1016/j.atmosenv.2012.12.013, 2013.

1577 Van Beelen, A., Roelofs, G., Hasekamp, O., Henzing, J., and Röckmann, T.: Estimation of
1578 aerosol water and chemical composition from AERONET Sun–sky radiometer measurements at
1579 Cabauw, the Netherlands, Atmos. Chem. Phys., 14, 5969-5987, https://doi.org/10.5194/acp-14-
1580 5969-2014, 2014.

1581 Wall, C. J., Norris, J. R., Possner, A., McCoy, D. T., McCoy, I. L., and Lutsko, N. J.: Assessing
1582 effective radiative forcing from aerosol–cloud interactions over the global ocean, Proceedings of
1583 the National Academy of Sciences, 119, e2210481119,
1584 https://doi.org/10.1073/pnas.2210481119, 2022.

1585 Wang, L., Lau, K.-H., Fung, C.-H., and Gan, J.-P.: The relative vorticity of ocean surface winds
1586 from the QuikSCAT satellite and its effects on the geneses of tropical cyclones in the South
1587 China Sea, Tellus A, 59, 562-569, https://doi.org/10.1111/j.1600-0870.2007.00249.x, 2007.

1588 Wang, S.-H., Welton, E. J., Holben, B. N., Tsay, S.-C., Lin, N.-H., Giles, D., Stewart, S. A.,
1589 Janjai, S., Nguyen, X. A., and Hsiao, T.-C.: Vertical distribution and columnar optical properties
1590 of springtime biomass-burning aerosols over Northern Indochina during 2014 7-SEAS
1591 campaign, Aerosol and Air Quality Research, 15, 2037-2050,
1592 https://doi.org/10.4209/aaqr.2015.05.0310, 2015.

1593 Wu, M.-c., and Choy, C.-w.: An Observational Study of the Changes in the Intensity and Motion
1594 of Tropical Cyclones crossing Luzon, Tropical Cyclone Research and Review, 4, 95-109,
1595 https://doi.org/10.6057/2015TCRRh3.01, 2016.

1596 Xian, P., Reid, J. S., Atwood, S. A., Johnson, R. S., Hyer, E. J., Westphal, D. L., and Sessions,
1597 W.: Smoke aerosol transport patterns over the Maritime Continent, Atmos. Res., 122, 469-485,
1598 https://doi.org/10.1016/j.atmosres.2012.05.006, 2013.

1599 Xiao, N., Shi, T., Calder, C. A., Munroe, D. K., Berrett, C., Wolfinbarger, S., and Li, D.: Spatial
1600 characteristics of the difference between MISR and MODIS aerosol optical depth retrievals over
1601 mainland Southeast Asia, Remote Sensing of Environment, 113, 1-9,
1602 https://doi.org/10.1016/j.rse.2008.07.011, 2009.

1603 Xie, Y., Li, Z., Zhang, Y., Zhang, Y., Li, D., Li, K., Xu, H., Zhang, Y., Wang, Y., and Chen, X.:
1604 Estimation of atmospheric aerosol composition from ground-based remote sensing
1605 measurements of Sun-sky radiometer, J. Geophys. Res.- Atmos., 122, 498-518,
1606 https://doi.org/10.1002/2016JD025839, 2017.

1607 Yang, S., Lau, W. K., Ji, Z., Dong, W., and Yang, S.: Impacts of radiative effect of pre-monsoon
1608 biomass burning aerosols on atmospheric circulation and rainfall over Southeast Asia and
1609 southern China, Climate Dynamics, 59, 417-432, https://doi.org/10.1007/s00382-021-06135-7,
1610 2022.

1611 Yumul Jr, G. P., Cruz, N. A., Dimalanta, C. B., Servando, N. T., and Hilario, F. D.: The 2007 dry
1612 spell in Luzon (Philippines): its cause, impact and corresponding response measures, Climatic
1613 change, 100, 633-644, https://doi.org/10.1007/s10584-009-9677-0, 2010.

1614 Zhao, G., Di Girolamo, L., Dey, S., Jones, A. L., and Bull, M.: Examination of direct cumulus
1615 contamination on MISR-retrieved aerosol optical depth and angstrom coefficient over ocean,
1616 Geophysical Research Letters, 36, https://doi.org/10.1029/2009GL038549, 2009.

1617 Zhao, G., Zhao, C., Kuang, Y., Bian, Y., Tao, J., Shen, C., and Yu, Y.: Calculating the aerosol
1618 asymmetry factor based on measurements from the humidified nephelometer system, Atmos.
1619 Chem. Phys., 18, 9049-9060, https://doi.org/10.5194/acp-18-9049-2018, 2018.